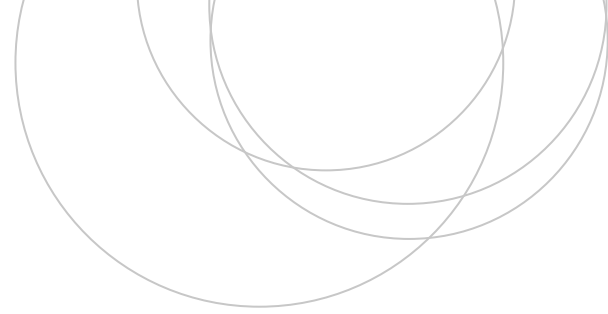




Universidad
del País Vasco

Euskal Herriko
Unibertsitatea

ZIENTZIA
ETA TEKNOLOGIA
FAKULTATEA
FACULTAD
DE CIENCIA
Y TECNOLOGÍA



Final Degree Dissertation (Electronic Engineering)
Double Degree in Physics and Electronic Engineering

PLANCK Satellite's Low Frequency Instrument: Study Of The Radiometers For Measuring The Cosmic Microwave Background (CMB)

Author:
Unai Arregi Leon
Director:
Joaquín Portilla Rubín

Motivation and acknowledgements

I have always been interested in the early Universe and when I heard about the Planck Mission I started gathering information about the CMB and its measurements. I found it exciting to have the chance to study how such a weak and ancient signal could have been measured with great accuracy and to analyse which the electronics behind all that stuff are. Moreover, the fact of being a double degree student has been advantageous: while the knowledge acquired in the Degree of Physics has allowed me to study all the mathematics and physics hidden in the CMB (see [5]), the Electronic Engineering Degree has let me analyse the high frequency electronic systems used for detecting such background radiation.

I would like to specially thank my parents and my twin Garazi because of the patience they have had during these 5 years, this could not have been possible without your help and love. I should also thank my grandparents, other relatives and of course my friends for making this way much easier. I am also thankful to my classmates (Paul, Garazi, Monfort, Sara, Kerdo, Miren, Leire, Irati, Beñat, Joseba, Izaro...) because I am sure that these years would have not been the same without them. Finally, I also thank my academic tutor and teacher Aitziber Anakabe because of being every single moment ready to listen to me and to help me whenever I needed. Thanks also to my teacher and director Joaquín Portilla; the simulations made in this work would have not been possible without his aid.

Motibazioa eta eskerrak

Betidanik izan dut Unibertso goiztiarraren inguruko interes handia eta Planck Misioaz lehenengoz entzun nuenean, aukera interesgarria iruditu zitzaidan bertan Mikrouhin Erradiazio Kosmikoa behatzeko erabilitako teknika lantzea. Gainera, gradu bikoitzeko ikaslea izanik aukera izan dut, alde batetik, Fisikako GrAL-ean CMB-aren atzean dagoen matematika eta fisika aztertzeko [5] eta, bestetik, Ingeniaritza Elektronikoko Graduan eskuratutako jakintzek hondoko erradiazio hau detektatzeko erabilitako goi maiztasuneko sistema elektronikoetan sakontzeko aukera eman didate.

Eskerrak eman nahi dizkiet bereziki nire gurasoei eta nire bixki Garaziri 5 urte hauetan izandako pazientziagatik, hau guztia ezinezkoa litzateke zuen laguntzarik eta maitasunik gabe. Eskerrak baita ere nire amona eta yeyeri, gainontzeko familiartekoei eta noski nire lagunei bidea errazagoa egiteagatik. Gelakideei ere eskerrak (Paul, Garazi, Monfort, Sara, Kerdo, Miren, Leire, Irati, Beñat, Joseba, Izaro...), 5 urte hauek ez bailirateke berdinak izango elkar ezagutu izan ez bagenu. Azkenik, eskerrak eman nahi dizkiot nire tutore akademikoa eta irakaslea izan den Aitziber Anakaberi, beti ni entzuteko prest egoteagatik eta behar izan dudana orotan lagundu izanagatik. Eskerririk asko baita Joaquín Portilla irakasle eta zuzendariari ere, lan honetako simulazioak ezinezkoak izango bailirateke bere laguntza eduki izan ez banu.

Contents

Motivation and acknowledgements	i
1 Introduction	1
2 The Cosmic Microwave Background (CMB): its origin, evolution and detection	2
3 Introduction to radiometry: overview and types of radiometers	5
3.1 Total power radiometer	7
3.2 The Dicke radiometer	11
3.3 The correlation radiometer	13
4 PLANCK mission: objectives, the spacecraft and its components	14
4.1 The Planck High Frequency Instrument (HFI)	15
4.2 The Planck Low Frequency Instrument (LFI)	16
4.2.1 Radiometer Array Assembly (RAA)	16
4.2.2 Sorption Cooler Subsystem (SCS)	19
4.2.3 Radiometer Electronics Box Assembly (REBA)	19
5 The Planck LFI radiometer: analytical model	20
5.1 Signal model	20
5.2 Pseudo-correlation radiometer sensitivity	24
5.3 Some systematic effects	26
5.3.1 Front-end amplifiers	27
5.3.2 Back-end amplifiers	27
6 Simulations with Advanced Design System (ADS)	29
6.1 Transient Envelope Analysis	29
6.2 Simulation results	31
6.2.1 Total power radiometer simulation	31
6.2.2 Pseudo-correlation radiometer simulation	36
7 Conclusions and outlook	40
References	

Chapter 1

Introduction

The Cosmic Microwave Background (CMB) has supposed an electromagnetic source of information for studying the properties of the early Universe, as well as for clarifying a wide range of uncertainties related to its thermal history and evolution. It is for these reasons that it has been of a great significance to measure such ancient radiation with high accuracy. In fact, a great deal of both ground and space experiments have been performed throughout history, where scientists have been facing formidable challenges in the sense of developing innovative techniques and making use of unprecedented instrumentation.

Radiometry is the scientific field that takes on the study of radio receivers, analyses their characteristics (sensitivity, resolution, signal model, circuitry...) and explores different measurement methods in order to obtain more and more rigorous results. It is in this sense that the Planck Mission from the European Space Agency (ESA) has been considered one of the biggest breakthroughs in the last years: it has been able to measure the CMB radiation with unique sensitivity and angular resolution, and has revealed both CMB temperature and polarization maps.

Hence our main objective is going to be to provide an overview of radiometry concepts and then focus on the so-called differential or pseudo-correlation radiometers used in the Planck Satellite. Besides, the particular case of the mentioned receptors will give us the opportunity to develop a specific analytical model for them, where our main goal will be to combine the theoretical results with simulation-based ones, strengthening in this way the successful performance and great utility of the technique employed in Planck Mission.

Concerning the structure of this work, in the upcoming second chapter we will give a general insight of the most important events through the Universe's thermal history in order to understand the origin of the CMB and its properties; moreover, we will also briefly mention some of the numerous experiments made for its measurement. Chapter 3 will be responsible for analysing different concepts of radiometry and presenting the most known radiometer types: the total power radiometer, the Dicke radiometer and the correlation radiometer. We will then be able to introduce ourselves in the study of the Planck Mission and the main features of its Low Frequency Instrument (LFI) will be explained (chapter 4). The analytical model of the LFI's pseudo-correlation radiometers will be developed in chapter 5, where we will also complete an analysis of systematic effects such as noise temperature and gain fluctuations. Chapter 6 will consist of simulations carried out with Advanced Design System (ADS) software: we will describe the simulation technique used and present the results achieved. The work will come to an end with some conclusions and future work discussion.

Chapter 2

The Cosmic Microwave Background (CMB): its origin, evolution and detection

The complete understanding of the Universe's thermal and evolutionary history is one of the most complex challenges cosmologists keep facing since long time ago. Nevertheless, all the theoretical work carried out in this scientific field together with the observational data obtained from different technological projects have led to an universal consensus: the Standard Cosmological Model or **Λ CDM model**. The latter is, by now, the theory which better fits the expected results coming from cosmological theories; in fact, it explains different aspects and properties of the observable Universe: its geometry, the necessity of an inflationary primordial period, the classification of matter components and their energy densities' evolution, the expansion rate, the values of a range of other cosmological parameters (Hubble's constant, optical depth...) and so long and so forth.

In this way, we may start with an overview of the history of the Universe based on the Λ CDM model in order to somehow justify which is the origin of the Cosmic Microwave Background (CMB): the study of the Planck Mission radiometers for the experimental characterisation of the CMB is, in fact, going to be the main objective of this work.

We can distinguish three different periods in Universe's thermal history, depending on the predominant matter component: radiation domination period, matter domination period and dark energy domination period. Just after the Big Bang happened, it is conjectured that the Universe was a very hot and dense entity, full of radiation. Thus, the cosmic plasma was composed of a mixture of the different relativistic particles existing at the moment (electrons, positrons, photons and the three neutrino species), which were in thermal equilibrium with one another. When the temperature reached the value of 1 MeV (remember that in cosmology we use the natural units $c = k_B = 1$), the neutrino decoupled from the cosmic plasma and the Universe kept expanding and, consequently, cooling. For temperatures lower than 1 MeV, the photons are not as energetic as in the previous ages, so that the reaction that keeps them in thermal equilibrium with the cosmic plasma, $e^+ + e^- \longleftrightarrow \gamma + \gamma$, will not be bidirectional so that electrons and positrons are annihilated. When reaching temperatures of order of 0.1 MeV, most of the neutrons join the protons in order to form the first light nuclei, while photons and electrons still keep interacting strongly [27].

The Universe continued cooling and it is not until the temperature of 0.75 eV that the radiation matter density equals the matter (i.e. baryonic matter and electrons) energy density [35]. From this point on, the Universe enters the so-called **matter dominated age**. When it comes to this work, we may say

that it is this period that covers the most part of our attention. In fact, as the temperature goes down, the number of free electrons decays (electrons and protons recombine) and the photons will less probably scatter with them. At a temperature of around 0.26 eV, it can be considered that photons will have no interaction with the cosmic plasma so that they expand freely and the Universe becomes transparent or visible [5]: this is known as photon decoupling.

Indeed, they are those free photons the ones that have been captured nowadays and that form the CMB. At photon decoupling, Universe is more or less 380000 years old and so it is evident that this radiation comes from really far points: we define the Last Scattering Surface (LSS) as the enormous spherical surface, centered in our galaxy, that plays the role of the source of the CMB photons that have been detected [1]. Since Universe is expanding, the physical distances are getting larger in time and so do the distances photons have travelled: this is the reason for which the detected photons' wavelengths (emitted at last scattering) have been redshifted and nowadays (almost 14 billion years after) are part of the microwave range in the electromagnetic spectrum.

Event	Age	Temperature
Neutrino decoupling	1 s	1 MeV
e^+e^- annihilation	6 s	0.5 MeV
Nuclei formation	180 s	0.1 MeV
Matter-Radiation equality	60000 years	0.75 eV
Recombination	260000 years	0.33 eV
Photon decoupling	380000 years	0.26 eV
Reionization	$400 \cdot 10^6$ years	2.6 meV
Dar energy-Matter equality	$9 \cdot 10^9$ years	0.33 meV
Nowadays	$13.8 \cdot 10^9$ years	0.24 meV

Table 2.1: Most important events of Universe's thermal history [7].

But, how did researchers discover this radiation? In 1965, the radio astronomers A. Penzias and R. Wilson, who were investigating the origin of radio interferences, found a really weak background noise at a frequency of 4 GHz (see figure (2.1)). This emission seemed to be unpolarized and isotropic (in other words, there was neither a preferred point nor a preferred special direction) [39]. In this way, although many speculations were made about the origin of this signal, in the same year the scientist Dicke published an article proposing the solution to this uncertainty: that signal, corresponding to a blackbody temperature of about 3K, was coming from a Hot Big Bang. They had discovered the CMB radiation. It was thanks to this work that A. Penzias and R. Wilson were awarded the **Nobel Prize in Physics** in 1978. However, at that time it was not still exactly clear to what extent was the detected radiation homogeneous and isotropic.

Further work has been done in this area since the first discovery of the CMB photons. As cosmolo-

gists were working on the origin of the structure formation (galaxies, clusters, etc...), they concluded that the observable inhomogeneous structures that form nowadays our observable Universe are a direct result of primordial density fluctuations. In addition, these fluctuations must have had a direct effect on the background radiation: the blackbody spectrum may present small temperature perturbations coming from different sky directions (they are defined as **CMB anisotropies**).

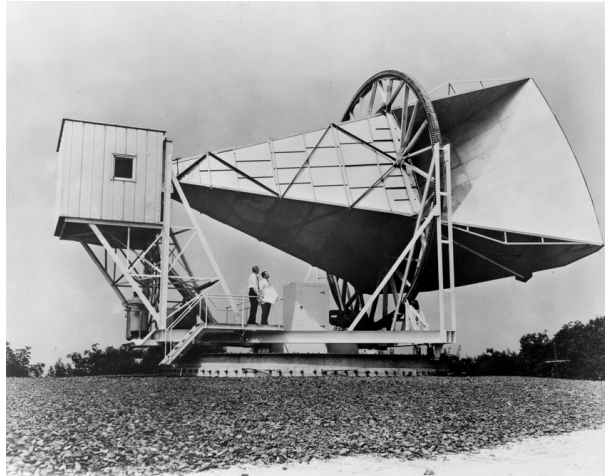


Figure 2.1: The horn antenna used by A. Penzias and R. Wilson in the year 1964 [31].

It was not until 1992 that these anisotropies were first found: it was on April of that year that the scientific group of the **COBE** (Cosmic Background Explorer) mission from NASA announced their discovery. Despite the fact of this great finding, the angular resolution of the COBE was low and the noise due to its instrumentation (it included a differential microwave radiometer together with a spectrophotometer and a diffuse infrared background experiment) was very large [12]. Therefore, many efforts were made for a better performance of instrumentation, with the aim of improving both sensitivity and angular resolution. In this way (while other ground experiments were carried out), in June 2001 NASA launched the **WMAP** (Wilkinson Microwave Anisotropy Probe) spacecraft, which observed the sky in five frequency bands (ranging from 20 GHz to 94 GHz) using passively cooled radiometers [12]. WMAP confirmed, among others, the almost flat spatial geometry of the Universe, the dark energy domination and the fact that the structures observed nowadays are the direct result of primordial nearly scale-invariant quantum fluctuations.

Apart from the temperature anisotropies, there was also a need for collecting information about CMB polarization in order to constrain the various cosmological models existing at the moment and the values of their parameters. Although WMAP delivered the first polarization data, the **PLANCK** Mission (launched on May 2009) of the European Space Agency (ESA) has been the successful successor to it: Planck satellite has mapped both the temperature and polarization of the sky with unprecedented sensitivity and angular resolution [16], covering the 30 GHz to 857 GHz frequency range. The Planck satellite contains two instruments (the Low Frequency Instrument (LFI) and the High Frequency Instrument (HFI)), and it is precisely the combination of the data obtained from each of them that provides Planck a great control of different systematic effects related to foreground emissions, instrumentation noise and other kind of limitations.

Before introducing ourselves in the detailed analysis of the Planck Mission (the spacecraft, the LFI and the electronics behind it, etc), we shall make an introduction to the different radiometer types used in radio astronomy and a brief study of their properties and the most important advantages/disadvantages.

Chapter 3

Introduction to radiometry: overview and types of radiometers

A radiometer is a device for the measurement of the radio frequency power corresponding to an electromagnetic emission coming from a certain source. The order of power of signals radiometers usually have to deal with ranges from 10^{-16} to 10^{-20} Watts [24] and they can be characterised as white noise signals: their power spectral density is constant (i.e. the same for all frequency components) and two signal values detected at different time instants are not statistically correlated (and, consequently, the autocorrelation function or the expectation value of the product between those two signals results to be proportional to the unit impulse function δ).

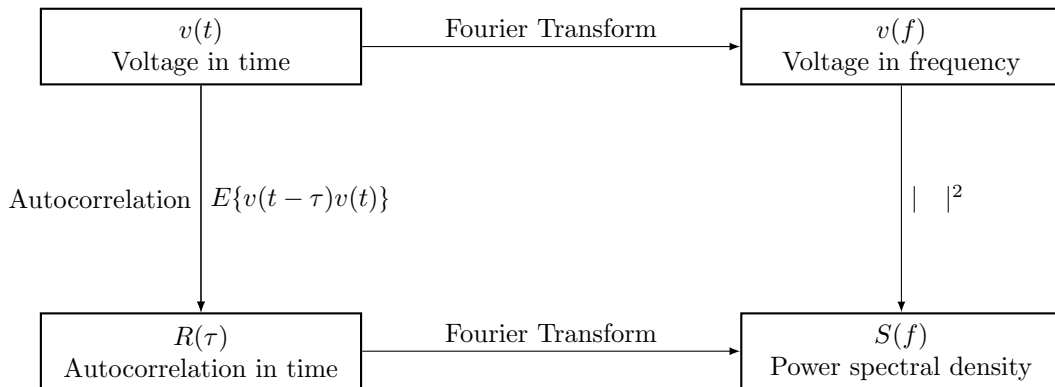


Figure 3.1: A simple scheme of the relationship between time domain and frequency domain magnitudes [38].

In addition, it should be noted the fact that these radio signals are commonly parameterised by their equivalent temperature. From Planck's law we do know that a body in thermodynamic equilibrium at temperature T irradiates energy; in the microwave region, the power such body emits is equal to $k_B BT$, where k_B is Boltzmann's constant and B is the bandwidth of the receiver [37]. Hence, in the particular case of radiometers' antennas, if we define the antenna temperature T_A as the effective antenna noise temperature that gathers different contributions as the background noise of the sky, the atmospheric noise or the antenna losses, the power collected by the antenna will be:

$$P_A = k_B BT_A. \quad (3.1)$$

The **sensitivity** of the radiometer is defined as the smallest change of the antenna temperature that can be detected at the output of the radiometer. As mentioned before, the power levels related to these temperatures are very low, and so the smallest detectable temperatures come to be limited by noise fluctuations that have its origin in the radiometer's circuits. Indeed, the radiometric power is usually less than the receiver's noise power. It is for this reason that it is crucial for radio astronomers to ensure that the following main conditions are fulfilled: on the one hand, the sensitivity must be high and, on the other hand, stability must also be required. These properties will enable us to distinguish the noise fluctuations introduced by the electronics from the real physical signal we are interested in.

Before analysing the most important radiometer types, we may see a general expression for the radiometers' sensitivity and see which the effect of instability is on it. The sensitivity or the resolution with which the input signal can be measured is given by the following expression [24]:

$$\Delta T = \frac{T_{sys}}{\sqrt{B \cdot \tau}} = \frac{T_A + T_N}{\sqrt{B \cdot \tau}}, \quad (3.2)$$

where T_{sys} is the sum of the antenna noise temperature (T_A) and the equivalent noise temperature of the receiver itself (T_N), B is the radiometer's effective bandwidth in Hz and τ is the integration time (in seconds) of the low pass filter located in the receiver, which as the same time is inversely proportional to the postdetection bandwidth. The effective bandwidth is given by the next expression:

$$B = \frac{(\int_0^\infty G(f)df)^2}{\int_0^\infty (G(f))^2 df}. \quad (3.3)$$

In this last expression, $G(f)$ is the receiver's transfer function up to the detection stage as a function of frequency. The effective bandwidth B is different from the bandwidth defined by the commonly used 3 dB criterion. Although its exact value depends on both the type and order of the bandpass filter used, it is usually higher than that of the 3 dB bandwidth [43]: $B \simeq (1.5 - 2)B_{3dB}$.

Concerning instabilities, they may appear due to both **gain fluctuations** and **noise temperature fluctuations**. The influence of noise temperature on sensitivity has been shown in the ΔT expression we have studied above. When it comes to gain fluctuations (ΔG), they are small variations that occur in amplifiers due to thermal or semiconductor instabilities [2]. Thus, they will obviously add another noise contribution to the radiometer's output signal and, as a consequence, the minimum antenna temperature change detectable will be higher [38] (sensitivity will be lower, then):

$$\frac{\Delta T}{T_{sys}} = K \sqrt{\frac{1}{B \cdot \tau} + \left(\frac{\Delta G}{G}\right)^2}. \quad (3.4)$$

The parameter K in the expression above will depend on the particular method the radiometer uses for isolating the desired physical signal from other noise contributions. Indeed, the development of such methods has been one of the greatest challenges of instrumentation throughout history, and we have made use of this fact to classify different type of radiometers in the following subsections: the total power radiometer ($K = 1$), the Dicke radiometer ($K = 2$) and the correlation radiometer ($K = \sqrt{2}$).

At this point, we find it advisable to make a comment on the meaning of the constantly used sensitivity concept in radio receivers. In fact, when we mention the sensitivity in radiometry, we are referring to the resolution. In other words, our sensitivity is not the usual slope of the calibration curve of a device (as in sensors, for example). In this way, as said before, ΔT represents the minimum change of the input signal that is detectable by the device under test. And now the question is, what is considered to be "detectable"? Which is the value we should compare the minimum signal change with?

The following convention is held in radiometry for solving such uncertainty: the sensitivity of a radiometer is the signal which will give an output voltage DC component equal to the root means square (rms) value of the output power fluctuations induced by the system noise signal [43]. This idea is represented in the following figure (3.2).

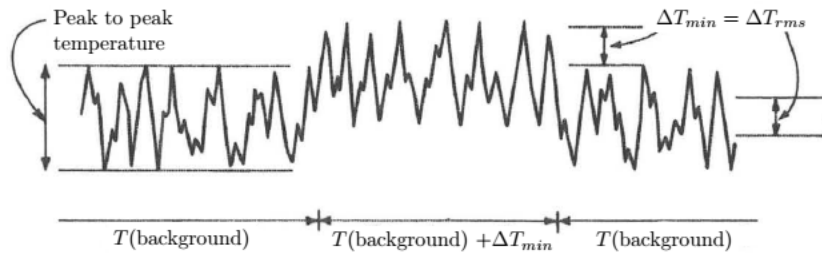


Figure 3.2: The graphical definition of sensitivity (resolution) of radio receptors [24].

Hence, the minimum measurable signal is considered to be detected when the output signal is enhanced by the same value as the effective voltage value corresponding to the fluctuations; or what is the same, when the total output power's rms value is the double of that belonging to the $T_{sys} = T_A + T_N$ signal. Therefore, as it can be observed in figure (3.2), the enhancement caused by the signal of our interest ΔT touches somehow tangentially with the fluctuating signal related to the system noise temperature: for this reason, ΔT is sometimes called *tangential sensitivity* in order to avoid confusions with the more common and widely spread meaning of "sensitivity". In this work, we will obviously always refer to the minimum detectable signal when using sensitivity or resolution terms.

The strategy followed in the following sections for obtaining the different sensitivities will be the one we have just outlined. Thus, our main goal will be to find the DC output change due to an input signal change and make it equal to the rms value of the output AC power component (also called variance):

$$\Delta v_{DC} = \sqrt{P_{AC}} \quad \longleftrightarrow \quad \Delta P_{DC} = P_{AC} . \quad (3.5)$$

3.1 Total power radiometer

Although the total power radiometer is not the most appropriate for the measurement of radio astronomical signals, the study of its performance will allow us to visualize which are the difficulties of the radiometer design. **The total power radiometer is the receiver that measures the total power signal coming from the antenna.** In order to study its characteristics, we ought to take a look to the block diagram of the total power receiver presented in the figure below.

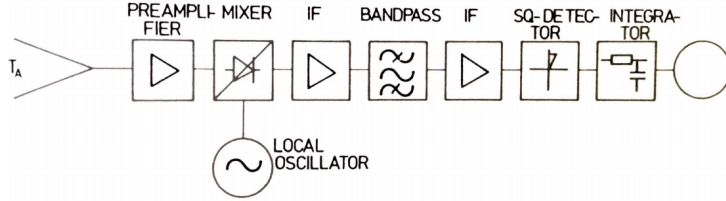


Figure 3.3: A representation of the block diagram of the total power radiometer [38].

As we can see, the detected input signal is mixed with a monochromatic oscillator signal produced locally (that is why it is also called the local oscillator). Thus, this mixer is responsible for performing a frequency conversion. Considering an ideal mixer, if we define the input signal frequency as f_{RF} and that of the local oscillator as f_{LO} , the output signal will contain information in two frequency components (with amplitudes proportional to the original antenna signal): $f_{RF} - f_{LO}$ (difference) and $f_{RF} + f_{LO}$ (sum). The difference frequency is called the intermediate frequency and we will consider this as the output signal of our interest: the upcoming stages (namely, the bandpass filter) will be designed to operate in this frequency (f_0).

Nevertheless, there exist two different input frequencies that result in the same equivalent mixer output frequency. On the one hand, if $f_{RF} = f_{LO} + f_0$, then the output of the mixer will belong to $f_{LO} + f_0 - f_{LO} = f_0$, as desired. But, on the other hand, in the case where $f_{RF} = f_{LO} - f_0$, the mixer output will be $f_{LO} - f_0 - f_{LO} = -f_0$. The latter response is called the image response of the mixer [11], and of course it is indistinguishable from the mixer's "direct" response. Consequently, the mixer will transform two different input frequency bands (located symmetrically with respect to f_{LO}) into the same intermediate frequency (f_0) band. The image or mirror frequency corresponding to the input f_{RF} will be the following one:

$$f_{im} = \begin{cases} f_{RF} + 2f_0 & f_{LO} > f_{RF} \\ f_{RF} - 2f_0 & f_{LO} < f_{RF} \end{cases} \quad (3.6)$$

In this way, for communication applications single band information measurements are usually required and so, the presence of the image response would lead to a confusion; in these cases, a filter for getting rid of the mirror frequency information would be desirable. However, in radiometry applications (as in our case), the signals are weak noise signals and, therefore, this double sideband performance turns out to be rather profitable. For this reason, the double sideband response of the total power radiometer will be considered in the following.

The antenna signal coming from the mixer output (together with the power that corresponds to the receptor's equivalent noise temperature itself) is amplified by a gain factor, let's say, G . Once amplified, the signal is passed through a bandpass filter with bandwidth B and the filtered power signal will directly be detected by a square-law detector. In this way, the output voltage of the detector will be proportional to the input filtered power. Finally, small fluctuations of the detected signal are smoothed by a low pass filter, which acts like an integrator with integration time τ_{LP} .

In order to understand the dependence of the minimum detectable temperature signal (or sensitivity) on the receiver's effective noise temperature (T_{sys}), it is useful to study the power spectral density of the signal along the different stages of the radiometer (see figure (3.1)). If we assume that the predetection part has an ideal rectangular passband of width B centered in the intermediate frequency f_0 , it is trivial

to affirm that the detector will be fed by a spectral power density of the same shape (see figure (3.4)).

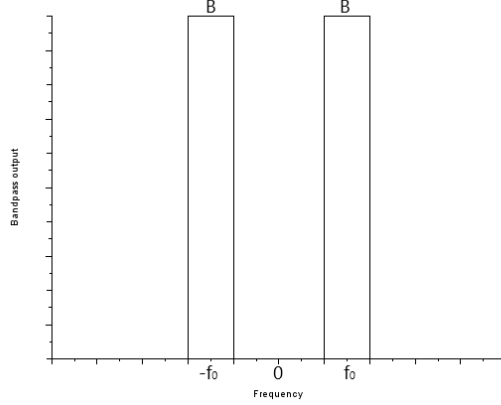


Figure 3.4: The power spectral density (PSD) in the output of the ideal bandpass filter.

Regarding the detection, the square-law detector relates in the following way its input and output signals: $y(t) = \alpha x^2(t)$. Now, taking into account that the input signal is a completely random Gaussian signal [38] (and, thus, with a null expectation value):

$$E\{x_1^2 x_2^2\} = E\{x_1^2\}E\{x_2^2\} + 2E^2\{x_1 x_2\}. \quad (3.7)$$

Thus, we can conclude the following relation between the input and output autocorrelation functions of the square-law detector (see (3.1) once more, where E denotes the expected value):

$$R_y(\tau) = \alpha^2 E\{x^2(t - \tau)x^2(t)\} = \alpha^2 (R_x^2(0) + 2R_x^2(\tau)). \quad (3.8)$$

Besides, as pointed in figure (3.1), the autocorrelation function and the power spectral density (PSD) form a Fourier transform pair. In this spirit, the Wiener-Khinchine Theorem is stated in the following way [47]:

$$S(f) = \int_{-\infty}^{\infty} R(\tau)e^{-j2\pi f\tau} d\tau \quad | \quad R(\tau) = E\{v(t - \tau)v(t)\}. \quad (3.9)$$

Hence, once the autocorrelation functions are known (equation (3.8)), we can take their Fourier transform (equation (3.9)) in order to obtain the relation between the input and output power spectral densities for the square law detector:

$$\begin{aligned} S_y(f) &= \alpha^2 R_x^2(0)\delta(f) + 2\alpha^2 \int_{-\infty}^{\infty} R_x^2(\tau)e^{-2\pi j f \tau} d\tau \\ &= \alpha^2 R_x^2(0)\delta(f) + 2\alpha^2 \int_{-\infty}^{\infty} S_x(f')df' \int_{-\infty}^{\infty} R_x(\tau)e^{-2\pi j(f-f')\tau} d\tau \\ &= \alpha^2 R_x^2(0)\delta(f) + 2\alpha^2 \int_{-\infty}^{\infty} S_x(f')S_x(f - f')df'. \end{aligned} \quad (3.10)$$

As one could have thought, the relation between the input and output PSDs is not the same as in linear systems ($S_y(f) = |H(f)|^2 S_x(f)$, where $H(f)$ is the transfer function of the linear system). As the square-law detector is a non-linear device, so must be the relation between S_y and S_x ; as we can see in

(3.10), at the output of the detector, we will have a DC component plus other AC components coming from the convolution integral. As S_x is the output PSD of the bandpass filter illustrated on (3.4) (i.e we will have the convolution between two square waves), the detector's output spectral density will contain the shape represented in figure (3.5).

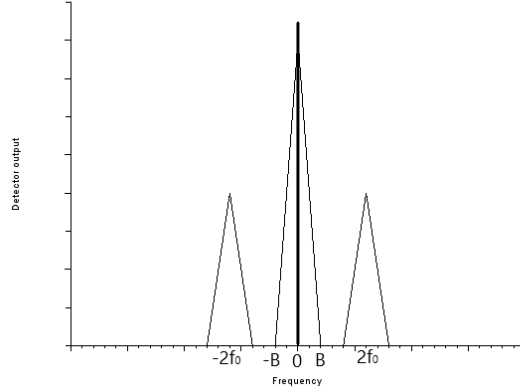


Figure 3.5: The output PSD (S_y) of the square-law detector. The shaded vertical line is the DC component. The three other triangular components are the direct result of the convolution of (3.4): we obtain two components of width B centered in $-2f_0$ and $2f_0$, and a double-height third component centered in 0 Hz of width $2B$.

It is this signal that is going to be filtered by the last low pass filter with effective bandwidth B_{LP} (much smaller than that of the predetection stage, B), the equivalent integration time of which being $\tau_{LP} = \frac{1}{2B_{LP}}$ [24]. The low pass filter will eliminate most of the random fluctuations and so the resulting output signal will contain the untouched DC component, together with a low frequency AC component determined by the filter's bandwidth.

Thus, we have qualitatively explained the behaviour of the signals corresponding to different stages of the total power radiometer. In order to obtain the expression of its sensitivity, we will now proceed to write the power components as a function of the physical measurable magnitudes. We define them in the following way:

- Sensitivity (minimum detectable temperature): ΔT
- Radiometer's equivalent noise temperature: $T_{sys} = T_A + T_N$
- Amplification stage's gain: G
- Detector's sensitivity: α

Therefore, on the one hand, taking into account all we mentioned above it is straightforward to see that the DC component of the detector's output power is (bear in mind that in our case the signals' PSDs are constant and equal to $k_B T$):

$$P_{out_{DC}} = \left(\alpha \frac{1}{2} G k_B (\Delta T + T_{sys}) B \right)^2 . \quad (3.11)$$

The $1/2$ factor in equation (3.11) occurs because the power spectral density is in this chapter defined for

both positive and negative frequencies [47] (i.e. this factor comes up from the double sideband consideration). The DC output due to the system noise T_{sys} is usually balanced with an equal battery voltage [43]; hence, the actual value of the radiometer's DC output power is just the same as the individual contribution of ΔT in equation (3.11).

On the other hand, as the AC components of the detector's output power will be filtered by the last low pass filter seen in figure (3.3) and its bandwidth B_{LP} is smaller than that of the pre-detection bandpass filter (B), we are just interested in the low frequency power component we obtained from the convolution in figure (3.5). Its value after the low pass filtering stage, (for the case that $\Delta T \ll T_{sys}$) can be estimated as [43]:

$$P_{out_{AC}} = 2 \left(\alpha \frac{1}{2} G k_B (\Delta T + T_{sys}) \right)^2 B B_{LP} \simeq 2 \left(\alpha \frac{1}{2} G k_B T_{sys} \right)^2 B B_{LP}. \quad (3.12)$$

In this way, we can find the sensitivity of the total power radiometer by equating the output's DC power component due to exclusively the sky signal and the low frequency AC output power corresponding to the receiver's noise temperature fluctuations. Taking into account the expressions of the signals and the approximations justified above, such powers led to the next result:

$$\begin{aligned} \text{from (3.11)} \longrightarrow P_{DC_{sky}} &= \left(\alpha \frac{1}{2} G k_B \Delta T B \right)^2 & \text{and from (3.12)} \longrightarrow P_{AC_{noise}} &= 2 \left(\alpha \frac{1}{2} G k_B T_{sys} \right)^2 B B_{LP} \\ P_{DC_{sky}} = P_{AC_{noise}} &\longleftrightarrow \Delta T = T_{sys} \sqrt{\frac{2B_{LP}}{B}} = \frac{T_{sys}}{\sqrt{B \cdot \tau_{LP}}}. \end{aligned} \quad (3.13)$$

Therefore, we can see that the higher the integration time of the low pass filter, the smaller will the contribution of noise fluctuations to the output signal be. Finally, by adding to (3.13) the contribution of gain variations (bear in mind that they are not correlated¹), we obtain the general sensitivity expression quoted in the equation (3.4) in the first part of this chapter (K being equal to 1):

$$\frac{\Delta T}{T_{sys}} = \sqrt{\frac{1}{B \cdot \tau_{LP}} + \left(\frac{\Delta G}{G} \right)^2}. \quad (3.14)$$

In many cases, these gain fluctuations we have just added are, precisely, the largest error source of the total power radiometer.

3.2 The Dicke radiometer

In 1946, **Dicke introduced an alternative** for reducing the effect of gain instability. Gain fluctuations usually have a long time constant (higher than 1 second), and hence it is conceptually possible to minimise this variation error by switching the receiver's input between the antenna and a known noise source at a relatively high frequency (typically it has the value of 1 kHz [37]) so that the predetection stage's gain has no time to change. It is precisely this **continuous calibration method** the solution Dicke proposed, and its corresponding block diagram is shown in the figure (3.6).

It can be seen that the main body of the Dicke radiometer keeps being the same of the total power receiver, but the main difference is that the input signal is periodically alternated between T_A and a

¹In general, two noise sources are summed as it follows: $E\{n_{tot}^2\} = E\{(n_1 + n_2)^2\} = E\{n_1^2\} + E\{n_2^2\} + 2E\{n_1 n_2\}$. When uncorrelated, this sums up to: $E\{n_{tot}^2\} = E\{n_1^2\} + E\{n_2^2\}$.

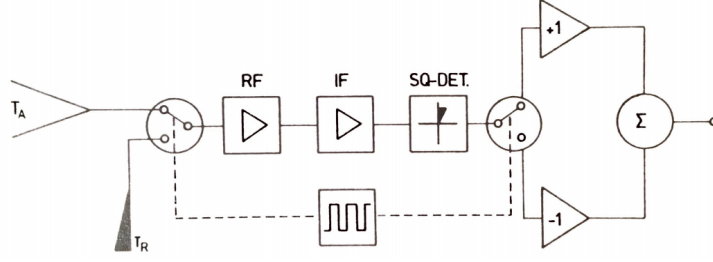


Figure 3.6: The simplified schematic block diagram of the Dicke radiometer [38]. Here the RF and IF stages represent respectively the same RF and IF blocks implemented in the total power radiometer of figure (3.3). The smoothing low pass filter will be implemented after the last adding section.

known reference T_R noise temperature.

In addition, after the input power has been detected by the square law detector, the signal is multiplied by $+1$ or -1 depending on the position of the Dicke switch by a phase-sensitive detector [24]. In this way, the output voltage signal will be proportional to T_A in one half period of the switching, and in the other half period it will be proportional to $-T_R$. Taking this into account, we can easily analyse how the effect of gain variations is reduced in this Dicke configuration radiometer; indeed, assuming that the receptor's equivalent noise temperature (T_N) does not change between the two switching states, we know that the output DC voltage of the receiver in a complete period will be the following:

$$V_{out} = \alpha G k_B (T_A - T_R) B. \quad (3.15)$$

So if we interpreted a gain fluctuation with a value of ΔG as a change on the output signal corresponding to an input antenna temperature variation of ΔT_G , we would obtain the following:

$$\alpha(G + \Delta G)k_B(T_A - T_R)B = \alpha G k_B(T_A + \Delta T_G - T_R)B \quad \longleftrightarrow \quad \Delta T_G = \frac{\Delta G}{G}(T_A - T_R). \quad (3.16)$$

Therefore, the contribution of gain fluctuations to the sensitivity ΔT turns out to be proportional to the temperature difference $T_A - T_R$, and not to the receiver's equivalent noise temperature (T_{sys}), as in the case of the total power radiometer [33].

Consequently, if the antenna temperature and the reference noise temperature are equal, the influence of gain variations on the output signal will completely be removed. Hence, in this case, the sensitivity or minimum detectable antenna temperature change of the Dicke radiometer will only be determined by the system equivalent noise:

$$\Delta T = \frac{2T_{sys}}{\sqrt{B \cdot \tau_{LP}}}. \quad (3.17)$$

We see that the minimum detectable antenna temperature change is the double (so, the sensitivity is the half) of that of the total power radiometer [24]: a factor of $\sqrt{2}$ comes from the fact that the antenna signal is measured in just one half period and the other $\sqrt{2}$ is due to the subtraction of the antenna and reference signals.

3.3 The correlation radiometer

The last type of radio receiver we are going to analyse is the so-called correlation radiometer. It is formed by two equal total power receivers, the outputs of which are multiplied so that the total output of the radiometer is proportional to the antenna signal. Note that the different noise power contributions to the output voltage will be null [41], since these are uncorrelated and their product's average vanishes. We show the block diagram related to the correlation radiometer in the figure below.

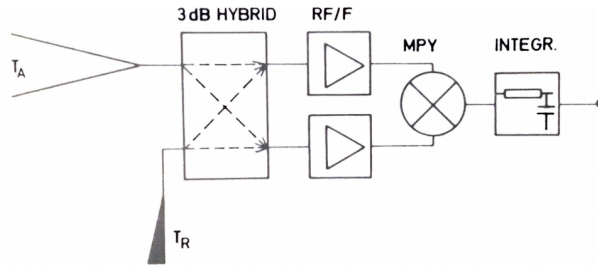


Figure 3.7: The schematic block diagram of the correlation radiometer [38].

In this way, in the first stage, the four-port hybrid device will generate two output signals: one branch will contain an output proportional to the sum between the antenna (sky) and reference load inputs, while the second branch's output will consist of a signal proportional to the difference of the mentioned two input signals. Afterwards, these outputs will be amplified by two equivalent RF stages, which finally will be multiplied between each other. Thanks to this multiplication and to the statistical properties of our noise signals, **the integrated output signal will just contain a signal proportional to the power coming from the antenna.**

Concerning the sensitivity of the correlation radiometer, as this kind of receivers allow to make continuous comparison and differentiation between both inputs of its two radiometric channels (each of them having a sensitivity equal to that of the total power radiometer), the minimum measurable signal shrinks by a factor of $\sqrt{2}$ in comparison of Dicke radiometer's sensitivity:

$$\Delta T = \sqrt{2} \frac{T_{sys}}{\sqrt{B \cdot \tau_{LP}}}. \quad (3.18)$$

The main disadvantage of this design may be the coupling and implementation of two identical receivers in parallel [43]. Notwithstanding, the correlation method or technique that distinguishes the correlation radiometer from other receivers, hence, enables us to improve significantly the sensitivity. Besides, other variations or alternative versions of the correlation receivers have been designed in order to minimise the effect of noise fluctuations introduced by instrumentation.

That is the case, for instance, of the radiometers used in the Low Frequency Instrument of Planck Satellite, which have supposed an extraordinary breakthrough in the field of radio astronomy instrumentation. In this way, we may introduce the main features of Planck mission in next chapter and, afterwards, we will focus on the detailed study of the Planck LFI differential or pseudo-correlation radiometers.

Chapter 4

PLANCK mission: objectives, the spacecraft and its components

As pointed in the previous sections, Planck was launched on May 2009 by the European Space Agency (ESA). The main objective of the mission was to deliver sky maps of both the temperature and the polarization of the redshifted cosmic microwave background photons coming from the last scattering surface. These satellite's design has enabled to obtain those maps in nine bands centered in the following frequencies: 30 GHz, 44 GHz, 70 GHz, 100 GHz, 143 GHz, 217 GHz, 353 GHz, 545 GHz and 857 GHz (speaking in a more correct way, it should be said that only the first three frequencies corresponding to the LFI instrument represent a central frequency; the other bands are covered by the High Frequency Instrument (HFI) and they are just identifier (reference) frequencies [3]). Furthermore, Planck mission had the challenging goal of testing out the wide range of theories that have been developed related to the Universe's birth, primordial time instants after Hot Big Bang and their evolution, by constraining the values of different cosmological parameters, detecting foreground emissions, etc.

In this way, a variety of experiments have been able to measure an average temperature of the sky of 2.726 K [21]. Although such temperature resolution might seem sufficient in a more somehow informal context, it should be pointed out that COBE already in the year 1992 (and, additionally WMAP nine years later) detected the intrinsic temperature fluctuations in the CMB at a level of $\frac{\Delta T}{T} = 10^{-5}$; hence, there is a great need for observing the sky in a much precise or sensitive way. In fact, this is precisely **one of the most important success of the Planck mission**: it has been able to measure the CMB anisotropies caused by primordial density perturbations with a sensitivity of around $2 \cdot 10^{-6}$ and an angular resolution reaching the value of $5'$ (i.e. 0.083°) [16].

The CMB fluctuations are theoretically described by their corresponding angular power spectrum, which holds all the information related to the particular cosmological model used. Therefore, the temperature maps can fully be characterised making use of a large sequence of correlation functions. As inflation predicts, the background radiation has Gaussian stochastic statistical properties, and so, the correlation functions are going to be two-point correlation functions or autocorrelation functions. Because the last scattering surface is a spherical surface, it is usual to expand the temperature fluctuations in spherical harmonics resulting in the following spectrum [30]:

$$R_T = \left\langle \frac{\delta T}{T}(\mathbf{l}_1) \frac{\delta T^*}{T}(\mathbf{l}_2) \right\rangle = \sum_l C_l \frac{2l+1}{4\pi} P_l(\cos \theta) \quad | \quad \mathbf{l}_1 \cdot \mathbf{l}_2 = \cos \theta, \quad (4.1)$$

where \mathbf{l}_1 and \mathbf{l}_2 are two different sky directions and the coefficients C_l are called multipoles. These multipoles are precisely the ones that have been measured with great accuracy by Planck Satellite and constitute a direct picture of the Universe at the age of last scattering (see figure (4.1)).

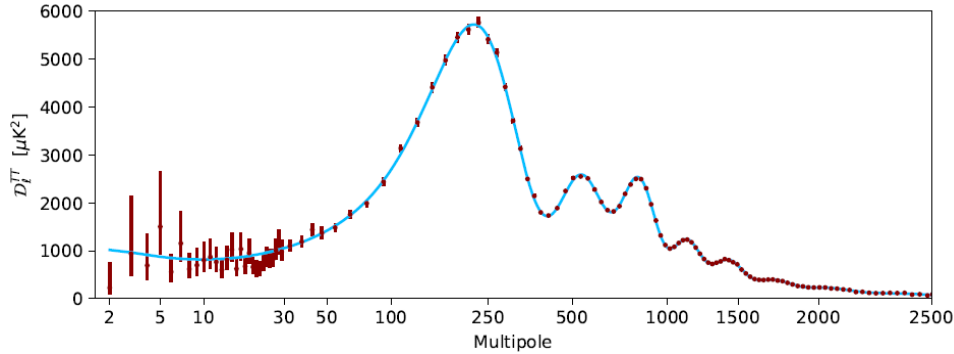


Figure 4.1: The angular power spectrum of the CMB temperature anisotropies measured by Planck [3]. The vertical axis corresponds to $D_l = l(l+1)C_l/2\pi$ and the horizontal axis represents the multipole l of the multipoles. The angular scale corresponding to a certain l is $\theta \simeq \pi/l$, so, the higher the multipole is, the smaller will be the angular scale corresponding to that particular anisotropy.

We will in the following describe the different units forming the Planck satellite that have been used for obtaining such results. Planck flew in a Lissajous orbit around the L2 Lagrangian point of the Earth-Sun subsystem, spinning at a rate of 1 rpm ($f = 0.017$ Hz) [8] around an axis 85° from the telescope boresight (i.e. from the telescope's maximum gain axis). The Planck satellite operated far beyond its baseline or nominal operating period of fifteen months: it was turned off on October 2013 having, thus, a total working period of 4.5 years and so had the option to complete **five full-sky surveys**, although the LFI did start its sixth survey due to its ability to work in higher temperatures than the HFI [20].

The Planck satellite contained two major modules [42]: the payload module (at 50 K) and the service module (at 300 K). The former consisted of an off-axis Gregorian type telescope with an effective diameter of 1.5 m, a telescope deflector, acting as both a light protector and a radiative cooler, and three thermal shields called V-grooves providing thermal isolation between satellite's cold parts and the warm module (these V-grooves are the principle components for passive-cooling, together with the telescope baffle mentioned above). The service module contained all the warm electronics (circuitry, the on-board computer, the telemetry components...) as well as the electrical power supplier and the cryogenic coolers that provide the cryogenic temperatures required for the proper performance of the LFI and the HFI.

4.1 The Planck High Frequency Instrument (HFI)

One of the most important contributions to Planck mission's success has come due to the wide spectral band covered. This would not have been possible without the two instruments integrated at the Planck focal plane: the HFI and the LFI.

The HFI was designed to obtain data from the frequency range above the spectral brightness peak of the CMB (located in a frequency of around 160.23 GHz or, equivalently, at a wavelength of 1.87 mm) at the six bands starting from that of 100 GHz mentioned in the first paragraph of this chapter. While the first four frequency channels were responsible for measuring the temperature and polarisation information of the CMB, the two highest bands were optimised to detect the foreground emissions and removing them from the desired background radiation signal [25].

The technology used by the HFI consisted of cryogenically cooled (namely at a temperature of 0.1 K) very sensitive 52 bolometers, which are a kind of incoherent receivers based on the effect that the resistance of a material is a function of temperature. Although the detailed study of them is beyond

the scope of this work, we could sum up its performance in a rather simple way. These bolometers are made of a conducting plate and a piece of semiconductor, which are in thermal contact with a cold bath; thus, when a CMB photon hits the bolometer, its temperature is changed and this change results in an equivalent change in its resistance [49].

4.2 The Planck Low Frequency Instrument (LFI)

Concerning the LFI, it covers the **30 GHz, 44 GHz and 70 GHz-centered frequency bands and makes use of an array of 22 differential radiometers** based on cryogenic indium phosphide (InP) high-electron-mobility transistor (HEMT) amplifiers, cooled at a temperature of 20 K. We show a general scheme of the LFI in the figure (4.2).

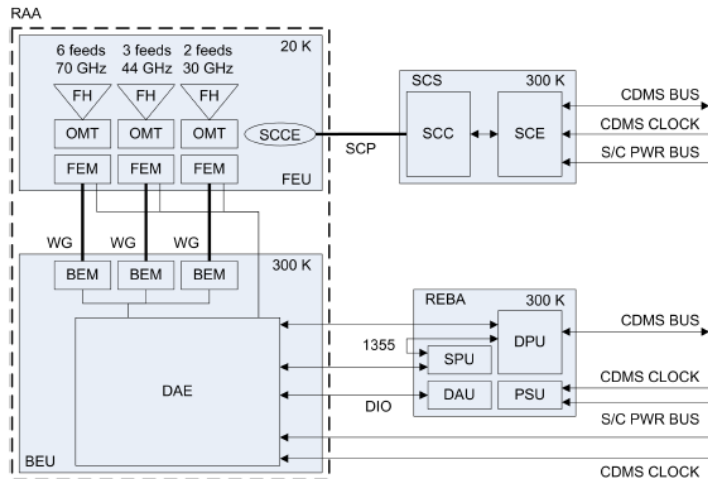


Figure 4.2: A schematic representation of the most important systems composing the Planck LFI [22].

As we can see, different subsystems of the LFI can be distinguished, each of them having a particular function: RAA, SCS and REBA.

4.2.1 Radiometer Array Assembly (RAA)

The background radiation coming from the sky feeds the LFI by 11 corrugated feed horns, each of which are connected to a double-radiometer system called the radiometer chain assembly (RCA). The RAA is precisely the ensemble of the 11 RCAs (2 at the 30 GHz channel, 3 at the 44 GHz channel and 6 at the 70 GHz channel) the LFI contains and it can be split up into the following subunits.

The Front End Unit (FEU)

The Front End Unit is composed by the Feed Horns, the Ortho-mode transducers and the Front End Modules.

- *Feed Horns (FHs)*: dual profiled corrugated horns are used in each RCA in order to collect the sky signal in the most appropriate way from the electromagnetic and the mechanical point of view. This dual profile consists of the mixture of an inner sine squared section starting from the throat ($R(z) \rightarrow z + \sin^2(z)$) and an outer exponential section near the aperture ($R(z) \rightarrow \exp(z)$) [44]. When it comes to the electromagnetic design of the FHs, the just described initial corrugated stage

that captures the sky signal enables the propagation of the electromagnetic field by the HE_{1n} hybrid modes. The HE_{11} is the fundamental mode (which at the same time can be represented as an in-phase combination of 85% TE_{11} and 15% TM_{11} smooth circular waveguide modes) and although it already stands for a nearly Gaussian mode, other higher order hybrid modes ($n > 1$) must be present in order to obtain a fundamental Gaussian beam mode at the horn aperture [10]. This goal is achieved by the optimization of different parameters of the dually profiled corrugations (period, width...).

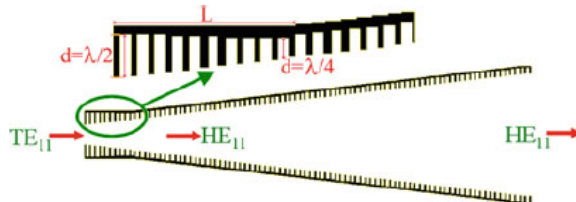


Figure 4.3: Impedance transformation at the throat of a corrugated horn [10]. In Planck LFI, the sky signal will be detected by the outer part of the horn and the radiation will be transmitted in the TE_{11} mode to the next stage, through the horn's throat.

Besides, the gradual transition stage between the corrugated guide and the smooth circular waveguide near the throat is based on the following technique (see figure (4.3)): the corrugation depth is smoothly reduced from $\lambda/2$ in the smooth part to $\lambda/4$ in the corrugated one, λ being the free space wavelength of the central frequency. In this way, the HE_{11} mode the horn's throat controls turns into the fundamental TE_{11} transversal electric mode of the smooth circular waveguide; its input radius is optimized in order to allow the dominant TE_{11} mode to be above cutoff frequency at the lowest usable frequency and to avoid the presence of the TM_{01} mode (which is the lowest order circularly symmetric mode of the circular waveguide [48]) below the highest operating frequency. This design provides very low RF losses [46].

- *Ortho-mode transducers (OMTs)*: the TE_{11} mode (suggesting that only the magnetic field has a non zero component along the propagation direction) coming from the feed horn's smooth circular guide is a polarization degenerate mode, since its field is circularly asymmetric [48]. The OMTs connected after the FHs are responsible for separating the incoming radiation into two orthogonal linearly polarised modes, TE_{10} and TE_{01} .

The OMT is a four port passive component [19]: its input's two ports are connected to the FH while the incoming signal is split up into two orthogonal components (one at each output port), feeding the LFI's radiometers. Concerning the design of the ortho-mode transducers [19], it consists of a first circular to square waveguide transition junction that transforms the input TE_{11} mode into the TE_{10} and TE_{01} square waveguide modes.

The adjacent square waveguide section is responsible for the correct establishment or fixing of the orthogonal modes, which are then separated into the two arms of the OMT: the main arm is responsible for the TE_{10} mode while the twisted side arm guides the TE_{01} mode (see (b) of figure (4.4)). Afterwards, each arm has a matching section between the TE square waveguide modes and the fundamental TE rectangular waveguide modes corresponding to the OMT arms. Finally, a geometrically stepped final stage enables the correct adaptation between the OMT and the LFI's front end modules.

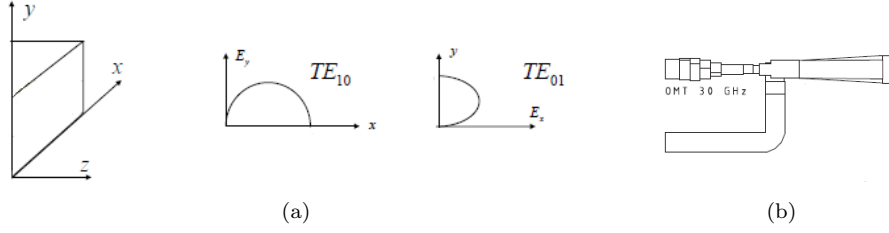


Figure 4.4: The left-side picture represents the TE_{10} and TE_{01} transverse electric modes of a rectangular waveguide. The right-side figure shows the OMT of the 30 GHz channel [19].

- *Front End Modules (FEMs)*: each RCA consists of two **pseudo-correlation radiometers**, the inputs of which are the two orthogonal linearly polarized sky signals and two other 4 K reference loads. As shown in the LFI's block diagram, the RCA is divided into a FEM (cooled at 20 K in order to get a lower noise temperature and a higher sensitivity) and a BEM (at 300 K). The FEM part of each RCA radiometer contains two 180° hybrids, two LNAs based on InP HEMT technology and two other phase shifters. Therefore, the sky and reference signals are coupled via the first 180° hybrid, and the resulting two output mixture signals are then amplified.

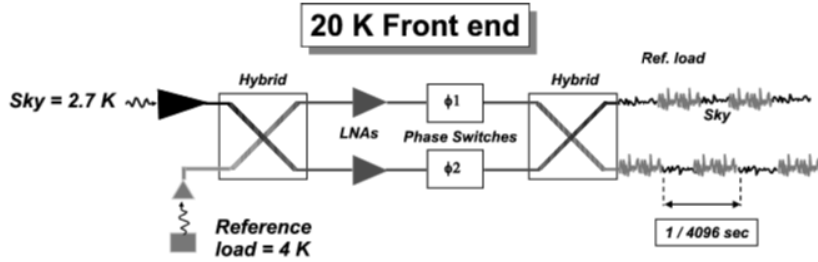


Figure 4.5: The Front End Module block diagram [28].

Two phase switchers are connected just before the second 180° hybrid stage: just one of them applies a phase change, whose value commutes between 0° and 180° at a rate of 4.096 kHz [9]; the phase shifter of the other radiometric branch is located for symmetry purposes. These phase switchers make use of two PIN diodes, controlled by their current and polarisation state [45, 17]; depending on their values, radiation travels directly to the second hybrid (0° phase shift) or $\lambda/2$ longer (180° phase shift). Finally, the RF amplified signals are once more coupled and, hence, the second hybrid's outputs will be proportional to the input sky and reference powers (see figure (4.5)).

Composite waveguides

The FEM's output signals are driven through 1.5-1.9 meters long rectangular waveguides to the Back End Module (BEM) entry, in order to ensure thermal isolation between both modules. So as to meet the desired electromagnetic, thermal and mechanical properties, two materials were used in the fabrication of the waveguides [18]: a first Copper section was built, followed by a Stainless Steel stage (partially gold plated for ohmic loss minimisation and mechanically and thermally connected to the V-grooves), as shown in the adjacent picture.

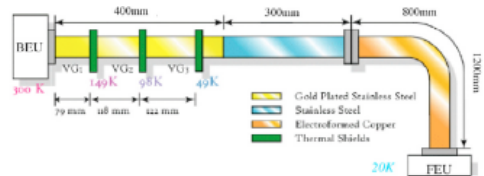


Figure 4.6: The structure of the composite waveguides [18]: gold plated steel (yellow), stainless steel (blue) and copper (orange).

The Back End Unit (BEU)

The last part of the RAA is the Back End Unit, constituted by the Back End Module (BEM) and the Data Acquisition Electronics (DAE) units.

- Back End Modules (BEMs): the incoming signals are firstly amplified by LNAs and filtered by band pass filters, which define the system's bandwidth. As seen in the developed introduction to radiometry, the next step is to detect the signal by a square-law detector so that the output voltage comes to be proportional to the input signal's power. It is precisely this voltage which will be amplified by a last low noise DC amplifier. Thus, the signals going to the next Data Acquisition Electronics stage will depend on the FEM's phase switch state: in one half period one of the two radiometric branches will contain the signal proportional to sky temperature while the other branch will carry the signal proportional to the reference 4K load; and in the other half period, the signals will change from one branch to the other (see the scheme shown in figure (4.7)).

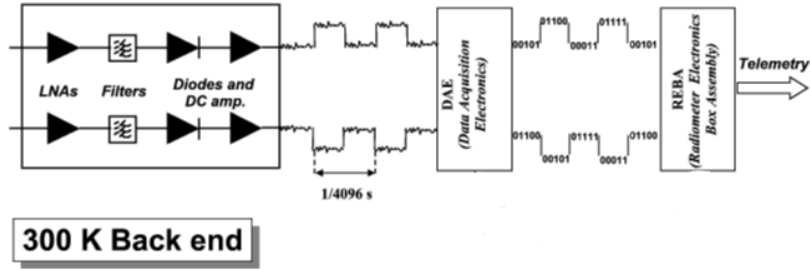


Figure 4.7: The Back End Module block diagram [28].

- Data Acquisition Electronics (DAE): this subsystem receives the square signals coming from the BEM and is responsible for integrating and digitalising all the information. Furthermore, the DAE does also contain extra subunits for other purposes such as power supply to RCAs and data storage in a RAM memory for a subsequent information recovery of the REBA [9] (see below).

4.2.2 Sorption Cooler Subsystem (SCS)

The SCS supplies the 20 K temperature needed by the LFI LNAs as well as the pre-cooling for both the 4 K cooler and the dilution cooler of the HFI [42]. The active cooling performed by the sorption cooler is based on hydrogen compression, gas cooling, Joule-Thomson expansion and final evaporation. Hence, not only does the SCS provide the maintenance of the two Planck instruments at their respective operating temperatures, but it also minimises vibrations and other thermal effects [29].

4.2.3 Radiometer Electronics Box Assembly (REBA)

The signals digitalised by the DAE are processed by the REBA. Hence, this subsystem is responsible for performing the extra signal averaging, data compression and telemetry packaging for the subsequent download for ground analysis [9]. Moreover, the REBA provides power supply for the LFI and contains the necessary units for RAA monitoring, overall data volume control, error management, etc.

Chapter 5

The Planck LFI radiometer: analytical model

When referring to the Planck LFI radiometers in the previous section, we used the concept of pseudo-correlation radiometers. Indeed, it is a modified version of the correlation radiometer explained in section (3.3): in the Planck LFI radiometers, one branch input is the sky signal while in the other branch we measure a reference load signal. In this sense, as both signals are coupled, we could think of a correlation radiometer; notwithstanding, the reference load temperature can be different from that of the sky signal resulting in an offset at the radiometer output. Of course, this difference between sky and reference load temperatures will be small, just a few K ($\simeq 1 - 2$ K).

So as to vanish the output signal, a **gain modulation factor** (r) is used [9]: once the detected signals are integrated and digitised by the DAE unit, the output corresponding to the reference load is multiplied by the factor r , making the difference ($v_{out_{sky}} - r \cdot v_{out_{ref}}$) as small as possible (see figure (5.1)). The multiplication of the gain modulation factor and the differentiation are made on Earth, once all the data has been compressed at the REBA and sent by telemetry.

As we will see in the following sections, the implementation of the gain modulation factor and the appropriate calibration of its value will not only lead to a considerable reduction of the sensitivity to both noise temperature fluctuations and LNAs' gain fluctuations, but it will also reduce the presence of the consequent $1/f$ noise at the output signal. This $1/f$ noise is defined as the noise whose power spectral density shrinks with frequency as $1/f$ (it is also called flicker noise), as we shall see in next sections. In fact, when it comes to the noise properties, the minimisation of $1/f$ noise strongly depends on the so-called post detection knee frequency (f_{knee}). The latter is defined as the frequency at which the ideal white noise (i.e. that of constant spectral density) contribution and the $1/f$ noise contribution are equal [40]. Thus, we will see that the effect of the back-end LNAs' gain fluctuations can effectively be suppressed by a correct choice of the relation between phase switching frequency and f_{knee} .

5.1 Signal model

In this section we are going to analyse the analytical expressions of the signals at different stages of the Planck LFI radiometers, in time domain. In the RF and microwave analysis, it is common to mathematically work with the so-called power waves: they represent voltages, whose squared absolute values result in the corresponding power. Our analysis will be a system-level analysis; in this way, let's consider the following transfer functions of the different devices of the radiometer's front- and back-ends [9]:

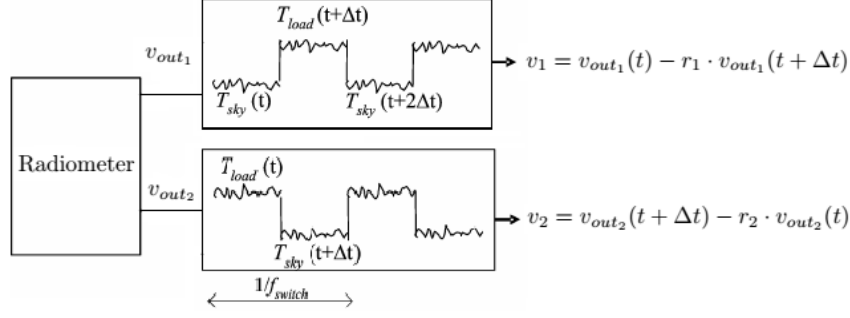


Figure 5.1: Radiometer outputs and gain modulation factor multiplication [2]. The time Δt corresponds to the half period of the switching: $\Delta t = 1/(2(4096Hz)) \simeq 122\mu s$.

$$f_{hyb} : \{x, y\} \rightarrow \left\{ \frac{x+y}{\sqrt{2}}, \frac{x-y}{\sqrt{2}} \right\} \quad (5.1)$$

$$f_{amp}^{FE} : \{x, y\} \rightarrow \{g_{F_1}(x + n_{F_1})e^{j\phi_{F_1}}, g_{F_2}(y + n_{F_2})e^{j\phi_{F_2}}\} \quad (5.2)$$

$$f_{switch} : \{x, y\} \rightarrow \left\{ x, \sqrt{A_i}e^{j\theta_i}y \right\} \quad \text{with } i = 1, 2 \quad (5.3)$$

$$f_{amp}^{BE} : \{x, y\} \rightarrow \{g_{B_1}(x + n_{B_1})e^{j\phi_{B_1}}, g_{B_2}(y + n_{B_2})e^{j\phi_{B_2}}\}. \quad (5.4)$$

The different parameters defined in the transfer functions have the next meaning [40]:

- $x(t)$ and $y(t)$ are the input voltages of the sky feed horn and the reference load horn.
- g_{F_1} , g_{F_2} and g_{B_1} , g_{B_2} are the voltage gains of the front-end and the back-end LNAs, respectively.
- $n_{F_1}(t)$, $n_{F_2}(t)$ and $n_{B_1}(t)$, $n_{B_2}(t)$ are the noise voltages introduced by the front-end and the back-end LNAs, respectively.
- ϕ_{F_1} , ϕ_{F_2} and ϕ_{B_1} , ϕ_{B_2} are the voltage phases introduced by the front-end and the back-end LNAs, respectively.
- A_1 and A_2 represent the fraction of the voltage amplitudes that are transmitted after the phase shifter (we have assumed that it is the switcher of the second branch which introduces the phase shift).
- θ_1 and θ_2 represent the phase shifts in the two switch states. We will take $\theta_1 = 0$ and $\theta_2 = \pi$.

Firstly, keeping these expressions in mind, we may write the output voltage signals of the Front Ends of the two radiometer branches as follows (as done in figure (5.1), we denote the upper radiometric branch as 1 and the lower branch as 2):

$$\text{Branch 1} \longrightarrow v_{out_{i1}}^{FE} = \frac{1}{\sqrt{2}} \left[e^{j\phi_{F_1}} g_{F_1} \left(n_{F_1} + \frac{x+y}{\sqrt{2}} \right) + \sqrt{A_i} e^{j(\theta_i + \phi_{F_2})} g_{F_2} \left(n_{F_2} + \frac{x-y}{\sqrt{2}} \right) \right] \quad (5.5)$$

$$\text{Branch 2} \longrightarrow v_{out_{i2}}^{FE} = \frac{1}{\sqrt{2}} \left[e^{j\phi_{F_1}} g_{F_1} \left(n_{F_1} + \frac{x+y}{\sqrt{2}} \right) - \sqrt{A_i} e^{j(\theta_i + \phi_{F_2})} g_{F_2} \left(n_{F_2} + \frac{x-y}{\sqrt{2}} \right) \right] \quad (5.6)$$

where, as in equation (5.3), the index i denotes the phase switch state. In this way, the FEs' output

signals of (5.5) and (5.6) pass through the Back End Modules, the voltages corresponding to the pre-detection section being:

$$\text{Branch 1} \longrightarrow v_{out_{i1}}^{BE-pre} = e^{j\phi_{B1}} g_{B1} (n_{B1} + v_{out_{i1}}^{FE}) \quad (5.7)$$

$$\text{Branch 2} \longrightarrow v_{out_{i2}}^{BE-pre} = e^{j\phi_{B2}} g_{B1} (n_{B2} + v_{out_{i2}}^{FE}) \quad (5.8)$$

These signals will then go straight to the square-law detector, resulting in the following BEs' output signals after additional DC amplification (see figure (5.1)):

$$\text{Branch 1} \longrightarrow v_{out_{i1}} = G_{DC1} \alpha_1 |e^{j\phi_{B1}} g_{B1} (n_{B1} + v_{out_{i1}}^{FE})|^2 \quad (5.9)$$

$$\text{Branch 2} \longrightarrow v_{out_{i2}} = G_{DC2} \alpha_2 |e^{j\phi_{B2}} g_{B1} (n_{B2} + v_{out_{i2}}^{FE})|^2 \quad (5.10)$$

Hence, taking into account the measurement technique explained in the introduction of this fifth chapter (see figure (5.1)), the final output signals will have the following analytical expression:

$$\text{Branch 1} \longrightarrow v_1 = v_{out_{i1}} - r_1 \cdot v_{out_{i2}} \quad (5.11)$$

$$\text{Branch 2} \longrightarrow v_2 = v_{out_{i2}} - r_2 \cdot v_{out_{i1}} \quad (5.12)$$

At this point, it is convenient to make some simplifying assumptions in order to develop the signals' expressions in a brighter and more comprehensive manner. On the one hand, we will assume that both radiometric arms are perfectly balanced, so that:

$$\begin{aligned} G_{DC1} &= G_{DC2} = G_{DC}, \\ \alpha_1 &= \alpha_2 = \alpha, \\ r_1 &= r_2 = r, \\ g_{F1} &= g_{F2} = g_F \quad \text{and} \quad \phi_{F1} = \phi_{F2} = \phi_F, \\ g_{B1} &= g_{B2} = g_B \quad \text{and} \quad \phi_{B1} = \phi_{B2} = \phi_B, \\ A_1 &= A_2 = 1 \quad (\text{lossless phase switchers}). \end{aligned} \quad (5.13)$$

On the other hand, note that we have not set neither $n_{F1} = n_{F2} = n_F$ nor $n_{B1} = n_{B2} = n_B$ in the noise voltages introduced by the front-end and back-end LNAs. In fact, we cannot make such a rough imposition, because in this case we are treating white noise signals; **as they are not deterministic signals it is impossible to talk about their values at a certain time instant** and, furthermore, it makes no sense to fix the two noise voltages coming from two different devices as equal in a determined time moment. Therefore, it is rather important to bear in mind that when handling such noise signals what it is indeed profitable is to work with their averaged or expected square values (because they do have in common different statistical properties).

By the way, we are now able to develop the final expression for the radiometer branches' outputs. We will explain in detail the case for the first upper branch, even though the equivalent procedure must be followed and the same results obtained for the case of the lower second branch. So, for equation (5.11), we have the following:

$$\begin{aligned} v_{out_{i1}} &= G_{DC} \alpha |e^{j\phi_B} g_B (n_{B1} + v_{out_{i1}}^{FE})|^2 = G_{DC} \alpha g_B^2 (n_{B1} + v_{out_{i1}}^{FE}) (n_{B1} + v_{out_{i1}}^{FE})^* \\ &= \dots = G_{DC} \alpha g_B^2 \left[n_{B1}^2 + \frac{1}{2} g_F^2 n_{F1}^2 + \frac{1}{2} g_F^2 n_{F2}^2 + g_F^2 x^2 \right] + \\ &+ G_{DC} \alpha g_B^2 \left[\sqrt{2} n_{B1} \cos(\phi_F) g_F (n_{F1} + n_{F2} + \sqrt{2}x) + \sqrt{2} g_F^2 x (n_{F1} + n_{F2}) + g_F^2 n_{F1} n_{F2} \right], \end{aligned} \quad (5.14)$$

$$\begin{aligned}
v_{out_{21}} &= G_{DC}\alpha |e^{j\phi_B} g_B (n_{B_1} + v_{out_{21}}^{FE})|^2 = G_{DC}\alpha g_B^2 (n_{B_1} + v_{out_{21}}^{FE}) (n_{B_1} + v_{out_{21}}^{FE})^* \\
&= \dots = G_{DC}\alpha g_B^2 \left[n_{B_1}^2 + \frac{1}{2}g_F^2 n_{F_1}^2 + \frac{1}{2}g_F^2 n_{F_2}^2 + g_F^2 y^2 \right] + \\
&+ G_{DC}\alpha g_B^2 \left[\sqrt{2}n_{B_1} \cos(\phi_F)g_F(n_{F_1} - n_{F_2} + \sqrt{2}y) + \sqrt{2}g_F^2 y(n_{F_1} - n_{F_2}) - g_F^2 n_{F_1} n_{F_2} \right].
\end{aligned} \tag{5.15}$$

Ergo the output voltage v_1 will be of the following form:

$$v_1 = G_{DC}\alpha g_B^2 g_F^2 \left[(1-r) \frac{n_{B_1}^2}{g_F^2} + \frac{1}{2}(1-r)n_{F_1}^2 + \frac{1}{2}(1-r)n_{F_2}^2 + x^2 - ry^2 + \mathcal{O}(X) \right], \tag{5.16}$$

where we have denoted as $\mathcal{O}(X)$ the terms consisting of the cross correlations between the different noise voltage signals coming from different sources (i.e. the contributions of the second brackets in equations (5.14) and (5.15)). The reason for summing up this cross terms is that when we take the time average of the output obtained in equation (5.16), as the different noise signals are uncorrelated, $E\{n_i n_j\} = \langle n_i n_j \rangle = \langle n_i \rangle \cdot \langle n_j \rangle$ will be equal to zero and will make no contribution to the averaged output voltage of the radiometer.

As far as the time averaging is concerned, we shall take the time average of (5.16) integrated over the bandwidth of the radiometer's bandpass filter's effective bandwidth B , as suggested in [40]:

$$\langle v_1 \rangle = \int_B \int_{\Delta t} v_1 dt df. \tag{5.17}$$

This will give us the DC voltage available at the output of the radiometer. Regarding equation (5.16), we may set the quadratic mean value of a white noise contribution as $\langle n_i^2 \rangle = k_B B T_i$ (of course, also for the contributions coming from the sky signal x^2 and the reference signal y^2), T_i being the equivalent noise temperature. Consequently, we obtain the following result:

$$\langle v_1 \rangle = G_{DC}\alpha g_B^2 g_F^2 k_B B \left[T_x + \frac{T_B}{g_F^2} + \frac{1}{2}T_{F_1} + \frac{1}{2}T_{F_2} - r \left(T_y + \frac{T_B}{g_F^2} + \frac{1}{2}T_{F_1} + \frac{1}{2}T_{F_2} \right) \right]. \tag{5.18}$$

As mentioned early, knowing the square mean values of noise signals will be advantageous for us. In fact, at this point, we can add a last assumption to our analytical model: we are now allowed to assume that the equivalent noise temperatures of the front-ends of both radiometric branches are equal, $T_{F_1} = T_{F_2} = T_F$. And so our last result becomes:

$$\langle v_1 \rangle = G_{DC}\alpha g_B^2 g_F^2 k_B B \left[T_x + \frac{T_B}{g_F^2} + T_F - r \left(T_y + \frac{T_B}{g_F^2} + T_F \right) \right]. \tag{5.19}$$

The development of the signals of the second radiometric leg would lead to the same result of equation (5.19) for $\langle v_2 \rangle$. We now can conclude which is **the proper value** we should adjust the gain modulation factor r to, in order to null the outputs $\langle v_1 \rangle$ and $\langle v_2 \rangle$:

$$\langle v_i \rangle = 0 \quad \longleftrightarrow \quad r = r_0 = \frac{T_x + \frac{T_B}{g_F^2} + T_F}{T_y + \frac{T_B}{g_F^2} + T_F} = \frac{T_x + T_N}{T_y + T_N}. \tag{5.20}$$

Remark that we have defined the receiver's equivalent noise temperature as $T_N = \frac{T_B}{g_F^2} + T_F$. As we could have expected, the front-ends' equivalent noise temperature has a greater importance than that of the back-end modules. Whereas the former undergoes both the FE and BE amplification stages, the latter just experiences the last back-end amplification; saying it in other words, the signal to noise ratio

($SNR = \frac{P_{signal}}{P_{noise}}$) will worsen (thus, will get smaller) due to the noise added by the radiometer's devices, being the first stages' noise figures the main (though not the only) responsables for such deterioration¹.

On top of that, the proper value of the gain modulation factor $r = r_0$ will not only null the output voltage signal of the radiometric branches, but it will also (as we shall see in the sections below) suppose the suppression of the sensitivity to gain fluctuations of the front end LNAs. Thus, **in the case of the FE amplifiers, the radiometer will only be sensible to the $1/f$ flicker noise caused by their equivalent noise temperature fluctuations.**

5.2 Pseudo-correlation radiometer sensitivity

Our next objective is going to be to reach the expression of the Planck LFI radiometers' sensitivity. As noted in chapter 3, on the one hand, we need to evaluate the change observed at the output DC voltage and, on the other, we may get to know which is the voltage corresponding to the output power's fluctuating component after integration.

Change in the output DC voltage

So as to determine the change in the output signal induced by an input sky temperature change, we will make use of the expression obtained in equation (5.19). As the low pass filter will not change the DC component, we get the following result according to the mentioned expression²:

$$\frac{\Delta\langle v_i \rangle}{\Delta T} = \frac{\partial [G_{DC} \alpha k_B B g_B^2 g_F^2 [T_x + T_N]]}{\partial T_x} = G_{DC} \alpha k_B B g_B^2 g_F^2 \quad \rightarrow \quad \Delta\langle v_i \rangle = G_{DC} \alpha k_B B g_B^2 g_F^2 \Delta T. \quad (5.21)$$

Effective value of the fluctuating AC power

For determining the rms value of the output variance (denoted by P_{AC}), we will follow the next steps: we will obtain the power spectral density ($S_{AC}^{pre-int}$) corresponding to the pre-integration stage output signal, we will then calculate the effect of the low pass filter and finally we will integrate the resulting PSD over all frequencies.

Hence, the fact that our signals are white noise signals will be of great aid for the simplification of the next calculations. Indeed, as we said in the first chapters of this work, these radio astronomical signals are characterised by their constant (frequency independent) power spectral density: $k_B T$ (in units of Watt/Hz). So, as the PSD is by definition the power amount measured per unit Hz, we can conclude that the $S_{AC}^{pre-int}$ takes the next form (remember the expression concluded for the AC fluctuating component in equation (3.10)):

$$S_{AC}^{pre-int} = \frac{v_{iAC}^2}{B} = \frac{[G_{DC}^2 2\alpha^2 k_B^2 B^2 g_B^4 g_F^4 [T_x + T_N]^2]}{B} = 2G_{DC}^2 \alpha^2 k_B^2 B g_B^4 g_F^4 [T_x + T_N]^2. \quad (5.22)$$

Next, we should account for the effect of the low pass filter or integrator. As it is a linear stage, the PSD of the filter's output signal will be the following one:

$$S_{AC} = |H(f)|^2 S_{AC}^{pre-int}. \quad (5.23)$$

¹This is stated by the Friis formula: $F = F_1 + \frac{F_2 - 1}{G_1} + \frac{F_3 - 1}{G_1 G_2} + \dots$ where F_1 is the noise figure of the first stage, G_1 the corresponding gain, and so on and so forth.

²Note that in this section we are working with the signals of the FE outputs and the DAE, and so, the gain modulation compensation will not be considered for sensitivity calculation: we will just focus on the signal of our interest, proportional to the sky temperature.

In our case, the integrator will just consist of a first order RC circuit, the transfer function of which being defined as:

$$H(f) = \frac{1}{1 + \frac{R}{Z_C}} = \frac{1}{1 + j2\pi f\tau_{RC}} \quad \rightarrow \quad |H(f)|^2 = \frac{1}{1 + (2\pi f\tau_{RC})^2} \quad | \quad \tau_{RC} = RC. \quad (5.24)$$

We shall now make a comment on the low pass filter's effective bandwidth B_{LP} used in chapter 3. This bandwidth is, as mentioned in that chapter, related as $B_{LP} = 1/2\tau_{LP}$ with the equivalent integration time τ_{LP} . Nevertheless, this equivalent integration time depends on the type and order of the filter used. For our one-pole RC circuit, this turns out to be [43]:

$$\tau_{LP} = 2\tau_{RC} = 2RC. \quad (5.25)$$

This relation supposes that the effective bandwidth B_{LP} is ~ 1.57 times the 3 dB bandwidth B_{3dB} [43]. Hence, the integrator's B_{LP} will be the following in our analysis:

$$B_{LP} = \frac{1}{2\tau_{LP}} = \frac{1}{4\tau_{RC}}. \quad (5.26)$$

Taking into consideration all we have said, we are now ready to calculate the fluctuating power coming from the integrator's output:

$$P_{AC} = \int_{-\infty}^{\infty} S_{AC} df = \int_{-\infty}^{\infty} |H(f)|^2 S_{AC}^{pre-int} df = S_{AC}^{pre-int} \int_{-\infty}^{\infty} |H(f)|^2 df. \quad (5.27)$$

In order to calculate the integral above, the use of the Parseval theorem [32] (i.e. the energy conservation: the energy in $H(f)$ equals the energy in the filter's impulse response $h(t)$) can be of great aid, according to which:

$$\begin{aligned} \int_{-\infty}^{\infty} |H(f)|^2 df &= \int_{-\infty}^{\infty} |h(t)|^2 dt = \int_{-\infty}^{\infty} |\mathcal{F}[H(f)]|^2 dt = \\ &= \int_{-\infty}^{\infty} \left| \frac{e^{-\frac{t}{\tau_{RC}}}}{\tau_{RC}} u(t) \right|^2 dt = \frac{1}{\tau_{RC}^2} \int_0^{\infty} e^{-\frac{2t}{\tau_{RC}}} dt = \frac{1}{2\tau_{RC}}, \end{aligned} \quad (5.28)$$

where \mathcal{F} denotes the Fourier transform operator and $u(t)$ is the unit step signal. In this way, equation (5.27) gives the following result:

$$P_{AC} = 2G_{DC}^2 \alpha^2 k_B^2 B g_B^4 g_F^4 [T_x + T_N]^2 \frac{1}{2\tau_{RC}} = 2G_{DC}^2 \alpha^2 k_B^2 B g_B^4 g_F^4 [T_x + T_N]^2 2B_{LP}. \quad (5.29)$$

We are now able to evaluate the condition (3.5) defined in chapter 3 for the case of the Planck LFI radiometers:

$$\begin{aligned} \Delta\langle v_i \rangle = \sqrt{P_{AC}} &\longleftrightarrow G_{DC} \alpha k_B B g_B^2 g_F^2 \Delta T = \sqrt{2} G_{DC} \alpha k_B \sqrt{B} g_B^2 g_F^2 [T_x + T_N] \sqrt{2B_{LP}} \\ &\longleftrightarrow G_{DC} \alpha k_B B g_B^2 g_F^2 \Delta T = \sqrt{2} G_{DC} \alpha k_B \sqrt{B} g_B^2 g_F^2 [T_x + T_N] \sqrt{\frac{1}{\tau_{LP}}}. \end{aligned} \quad (5.30)$$

And so, it is straightly seen that **the resulting sensitivity** is:

$$\Delta T = \sqrt{2} \frac{[T_x + T_N]}{\sqrt{B \cdot \tau_{LP}}}. \quad (5.31)$$

5.3 Some systematic effects

In order to finish the analytical model and the study of the Planck LFI radiometers, it may be interesting to analyse **the susceptibility they present to different parameter changes**. As done in the calculation of the output DC voltage ($\langle v_i \rangle$) change due to a sky temperature variation, we can generalise equation (5.21) to any other general varying magnitude λ . Therefore, if the output signal's fluctuation induced by a variation of the parameter λ is interpreted as a ΔT_{fluc} change in the radiometer's output [40]:

$$\frac{\partial \langle v_i \rangle}{\partial T_x} \Delta T_{fluc} = \frac{\partial \langle v_i \rangle}{\lambda} \Delta \lambda. \quad (5.32)$$

Particularly, as we will study the sensibility to the LNAs' gain and effective noise temperature fluctuations, we will have $\lambda = g_F^2, g_B^2, T_F$ (bear in mind that we are always working with power gains, i.e. g_i^2). Before entering such discussion, it might be helpful to characterise the noise spectra related to the mentioned gain and temperature fluctuations. In the case of the InP HEMT LNAs of the Planck radiometers, it has been proven that both gain and noise temperature variations present a **1/f spectrum** (i.e. their noise contributions are strong for low frequencies, as seen in figure (5.2)).

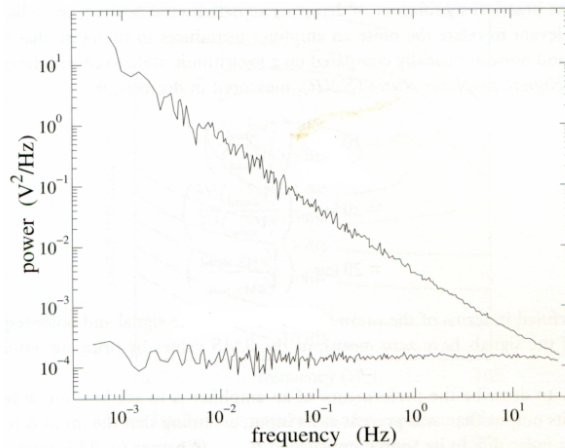


Figure 5.2: The noise power spectra corresponding to the white noise (lower horizontal signal) and the 1/f flicker noise (sometimes also called pink noise) [15], the latter being of great importance in low frequencies.

Hence, rewriting the power gains as $g_i^2 = G_i$, we will consider the following PSDs for gain and noise temperature fluctuations, respectively [40]:

$$\sqrt{S_{G_i}(f)} = \frac{\Delta G_i(f)}{G_i} = \frac{C}{\sqrt{f}}, \quad (5.33)$$

$$\sqrt{S_{T_i}(f)} = \frac{\Delta T_i(f)}{T_i} = \frac{A}{\sqrt{f}}, \quad (5.34)$$

where A and C are the normalization constants for each PSD, the relation between both of them being $A = C/(2\sqrt{N})$ (where N is the number of stages in the amplifier). We will study in the following subsections the different systematic effects related to the FE and BE amplifiers' parameters. Furthermore, we will analyse the influence of the gain modulation factor (r) on such effects and the constraints imposed by the knee frequency.

5.3.1 Front-end amplifiers

When it comes to the front-end amplifiers, we will first study the sensibility of the Planck radiometers to variations on their equivalent noise temperatures (we now have two varying parameters: $\lambda_1 = T_{F_1}$ and $\lambda_2 = T_{F_2}$). As both branches of the radiometers do include amplifiers, we will consider the expression of equation (5.18) for this first analysis. In this way, according to equation (5.32), the spurious signal fluctuation ΔT will be this³:

$$\begin{aligned}\Delta T_{fluc} &= \sqrt{\left(\Delta T_{F_1}(f) \frac{\partial \langle v_i \rangle / \partial T_{F_1}}{\partial \langle v_i \rangle / \partial T_x}\right)^2 + \left(\Delta T_{F_2}(f) \frac{\partial \langle v_i \rangle / \partial T_{F_2}}{\partial \langle v_i \rangle / \partial T_x}\right)^2} = \\ &= \sqrt{\left(\Delta T_{F_1}(f) \frac{1-r}{2}\right)^2 + \left(\Delta T_{F_2}(f) \frac{1-r}{2}\right)^2} = \\ &= \Delta T_F(f) \frac{1-r}{\sqrt{2}} = \frac{A}{\sqrt{f}} \frac{T_F(1-r)}{\sqrt{2}},\end{aligned}\tag{5.35}$$

where in the last line we have assumed that both noise spectra are equal⁴. According to the result we have obtained, we can say that the choice of $r = 1$ would lead to a suppression of the susceptibility to the FE LNAs' noise temperature fluctuations. What is more, we can also achieve the expression for the post-detection knee frequency at which the contribution of the $1/f$ noise from (5.35) equals the white noise spectra contribution we obtained in equation (5.31)⁵:

$$\Delta T_{fluc}(f = f_{knee}) = (\Delta T)_{(5.31)} \iff f_{knee}^{FE} = \left(\frac{T_F(1-r)A}{2[T_x + T_N]}\right)^2 B.\tag{5.36}$$

This last result enforces, thus, the fact that for $r = 1$ the radiometer would be insensitive to noise temperature fluctuations. Besides, we may also repeat the same analytical development for the case of front-end amplifiers' gain fluctuations. In such case:

$$\Delta T_{fluc} = \Delta G_F \frac{\partial \langle v_i \rangle / \partial G_F}{\partial \langle v_i \rangle / \partial T_x} = \frac{\Delta G_F}{G_F} [T_x + T_N - r(T_y + T_N)] = \frac{C}{\sqrt{f}} [T_x + T_N - r(T_y + T_N)].\tag{5.37}$$

Ergo it is observable that, as said in the signal model section of this chapter, the $r = r_0 = \frac{T_x + T_N}{T_y + T_N}$ choice that nulls the output signal (as we are interested) will also be responsible for the abolition of front-end amplifiers' gain instability effects. It is straightforward to see from equation (5.37) that **the knee frequency is proportional to $[T_x + T_N - r(T_y + T_N)]^2$ and so also vanishes in our preferred $r = r_0$ choice.**

5.3.2 Back-end amplifiers

Concerning the back-end LNAs, we shall just study the susceptibility to their gain variations. Indeed, we have seen that their equivalent noise temperatures are annihilated by the FE power gain G_F and their contribution will be negligible. Having said so, we will analyse the particular case where there is the presence of a BE gain fluctuation between the two phase switch states [40]. Therefore, our gain modulated output signal at each radiometric branch would be:

³Remember that both noise contributions will not be correlated.

⁴When adding noise contributions, we have to consider that we have two independent noise sources. However, after obtaining the final result, it makes sense to impose once more $T_{F_1} = T_{F_2} = T_F$.

⁵The spectra contribution of the sensitivity obtained in (5.31) is $\sqrt{\frac{2}{B}} [T_x + T_N]$, expressed in $K/\sqrt{\text{Hz}}$.

$$\begin{aligned}
\langle v_i \rangle &= \alpha k_B B G_F G_B [T_x + T_N] - r \cdot \alpha k_B B G_F (G_B + \Delta G_B) [T_y + T_N] = \\
&= \alpha k_B B G_F G_B \left[T_x + T_N - r \cdot (T_y + T_N) - r \cdot (T_y + T_N) \frac{\Delta G_B}{G_B} \right].
\end{aligned} \tag{5.38}$$

Thus, the ΔG_B fluctuation is imprinted as an equivalent temperature change in the output signal:

$$\Delta T_{fluc} = -r \cdot (T_y + T_N) \frac{\Delta G_B}{G_B} = -r \cdot \frac{C}{\sqrt{f}} (T_y + T_N). \tag{5.39}$$

Similarly, once we have obtained the expression for the spurious signal caused by the fluctuations, we can reach the post-detection knee frequency expression in order to analyse at which frequencies will back-end gain changes alter the physical signals we want to measure. Using, once more, the sensitivity result obtained in equation (5.31):

$$\Delta T_{fluc}(f = f_{knee}) = (\Delta T)_{(5.31)} \longleftrightarrow f_{knee}^{BE} = \frac{C^2 B}{2} = 2N_s A^2 B. \tag{5.40}$$

For the case of back-end gain variations within a complete phase-switching period, the corresponding knee frequency results in an important constraint. As its value in equation (5.40) is determined by the bandpass filter's effective bandwidth and the number of amplification stages, its typical order of magnitude using values from Planck mission ranges between 1 – 2 Hz [40]. Hence, **we should be sure that the phase switching period is fixed to be much faster than that of f_{knee}^{BE}** , so that G_B remains constant. Remember that in Planck LFI a switching period of 4.096 kHz was chosen, a value that results in a small back-end $1/f$ noise addition.

Chapter 6

Simulations with Advanced Design System (ADS)

In this sixth chapter we will explain the simulations carried out using Advanced Design System (ADS) software. The latter contains a RF simulator that not only does enable to study the performance of RF circuits, but it does also include a set of block-level RF models of linear and non-linear components, among others. In this way, we will make use of the so-called Transient Envelope simulation technique as well as a system-level analysis of radio receivers such as the total power radiometer and the pseudo-correlation radiometer.

6.1 Transient Envelope Analysis

The Transient Envelope assumes that the input signal can be expressed as the product between a carrier signal and an envelope in time domain. In this way, if we denote $x(t)$ as the modulated input signal and f_0 as the frequency corresponding to the carrier one, the following can be written [36]:

$$x(t) = a_x(t) \cos 2\pi f_0 t + \phi(t) = \Re[a_x(t)e^{j\phi(t)}e^{j2\pi f_0 t}], \quad (6.1)$$

where $[a_x(t)]e^{j\phi(t)}$ represents the envelope signal and $e^{j2\pi f_0 t}$ is the carrier signal. As the modulating or envelope signal can in general be complex, if we write it in the binomial notation as $[a_x(t)]e^{j\phi(t)} = p(t) + jq(t)$, equation (6.1) turns to¹:

$$x(t) = p(t) \cos 2\pi f_0 t - q(t) \sin 2\pi f_0 t. \quad (6.2)$$

Hence, it is this signal the one that will pass the particular system under study and the signal of interest can be recovered by subsequent demodulation. Let's now see which the steps followed by the **Transient Envelope (TE)** technique are. The main idea is that TE represents the input signal as a RF carrier in frequency domain, with a modulation envelope in time domain (i.e. is a hybrid time-frequency domain method).

Firstly, the envelope signal is sampled in time domain according to the time step fixed in the simulation setup, as it can be seen in figure (6.2). These sampled envelope values are then at each step passed through the RF system and the circuit's equations are solved using the **Harmonic Balance (HB)** method, which is also a hybrid time-frequency domain approach. The latter splits the whole circuit into its linear and non-linear subcircuits, and assumes that the output voltage can be written as a combination of the input signal's harmonics.

¹Remember Euler's formula: $e^{jx} = \cos x + j \sin x$

The HB method consists of the following algorithm [26] (see figure (6.1)): (i) an initial value for voltage is estimated, $v^{i=0}(t)$; (ii) the non-linear subcircuit is applied in time domain, and the result is converted into frequency domain via Fourier transform ($i_{nl}(\omega)$); (iii) the linear subcircuit is solved in frequency domain ($i_l(\omega)$), using $v^i(\omega)$; (iv) according to Kirchoff's Current Law (KCL) it is checked whether the linear and non-linear solutions are balanced or not: $f(v^i) = i_l(\omega) + i_{nl}(\omega) = 0$; if the convergence criteria imposed is not fulfilled, then an iterative method as, for instance, the Newton-Raphson method is used for updating the value of $v^i(\omega)$ to $v^{i+1}(\omega)$ and the process is restarted.

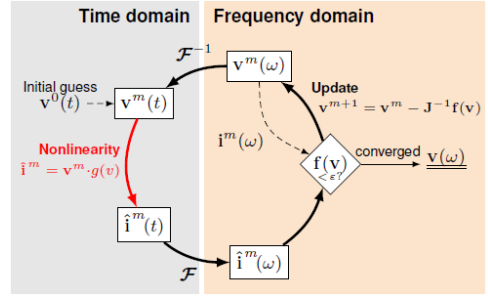


Figure 6.1: The algorithm of the Harmonic Balance method [26].

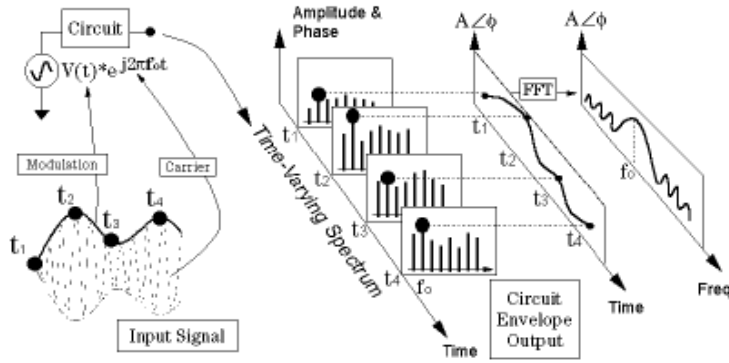


Figure 6.2: The Transient Envelope simulation technique [14].

Therefore, the HB method will give the steady-state solution of the output signal as a combination of the carrier's harmonics nf_0 , as represented in figure (6.2). As a consequence, taking into account all the solutions obtained at each time step, the TE analysis will provide the time varying amplitude-phase combination to the rythm of the envelope signal, around each harmonic of the carrier [36]. Hence, the spectrum around the desired harmonic can be obtained by applying the Fourier transform to the corresponding time-varying response (see, once more, figure 6.2). In this way, each nf_0 frequency can be thought as the central frequency of a spectrum with a bandwidth of $1/\text{TimeStep}$. This reveals the importance of setting **proper values for both time step and stop time** [14]:

- Time step: determines the bandwidth of the spectrum at the output and so, we need to fix a sufficiently small time step so that the highest frequencies are properly captured. $1/\text{TimeStep}$ should be at least twice the modulation bandwidth.
- Stop time: defines the duration of the time domain simulation. Moreover, the stop time determines the frequency resolution of the output spectrum: a sufficiently large stop time should be used in order to solve the spectral components of our interest.

Summing up, both the Harmonic Balance and the Transient Envelope simulation techniques are specially advantageous for RF circuits, as they entail an appropriate treatment of elements defined in the frequency domain. Nevertheless, the Transient Envelope method we will use in our ADS simulations is more efficient in terms of RAM and CPU requirements, as, among other reasons [14]: in TE the transient simulation is just made around the carrier and its harmonics and, additionally, the TE provides a time varying spectrum while the HB is limited to constant spectra.

6.2 Simulation results

In this section we are going to present the specifications we have imposed in our simulations and, afterwards, we will analyse the results obtained. As said before, we are going to make use of the Transient Envelope (TE) simulation technique. In our case, though, every signal comes to be a noise signal and so we will not have a carrier signal per se. Nevertheless, as our radiometers must represent receivers useful in a particular bandwidth around a certain central frequency, we are going to somehow mislead the ADS simulator and specify a carrier frequency of $f_0 = 30 \text{ GHz}$ (thus corresponding to the first band of Planck LFI) despite the fact that in our circuit there will not be any single-tone signal of 30 GHz.

Saying it in other words, we will exclusively work with noise signals, but we will analyse their behaviour around the $f_0 = 30 \text{ GHz}$ component and its harmonics. Having said so, we must now set the values for the **TE simulation parameters**: number of harmonics (n), bandwidth (B), time step (t_{step}) and stop time (t_{stop}).

The number of harmonics we have chosen is $n = 3$ (sufficient for our analysis) and the bandwidth we have set takes the value of $B = 300 \text{ MHz}$. It is true that in Planck Mission each frequency channel had a bandwidth of 20% (so for the 30 GHz channel, the $B = 6 \text{ GHz}$), but the 300 MHz choice will be enough for obtaining meaningful results in our simplified simulations. In addition, once the bandwidth has been fixed, we are in a position to fix the time step value too. Taking into account all we said before, the maximum time step results in:

$$\frac{1}{t_{step_{max}}} = 2 \cdot B \iff t_{step_{max}} = 1.67 \text{ nsec} . \quad (6.3)$$

Hence, we have chosen a more relaxed value of $t_{step} = 1 \text{ nsec}$. Finally, when it comes to the stop time, we have proven that in order to let the output signals reach their steady-state value and achieve an acceptable frequency resolution, a stop time of $t_{stop} = 7 \mu\text{sec}$ is a good choice. These values of the Transient Envelope parameters (see table below) will be used in all the upcoming simulations.

Parameter	Value
f_0	30 GHz
B	300 MHz
n	3
t_{step}	1 nsec
t_{stop}	7 μsec

Table 6.1: Values chosen for the Transient Envelope simulation parameters.

Let's now see which are the system-level circuits designed for the total power radiometer and the pseudo-correlation radiometer, as well as the corresponding results.

6.2.1 Total power radiometer simulation

We will first study the total power radiometer. The figure representing the schematic circuit is shown in the following picture (6.3).

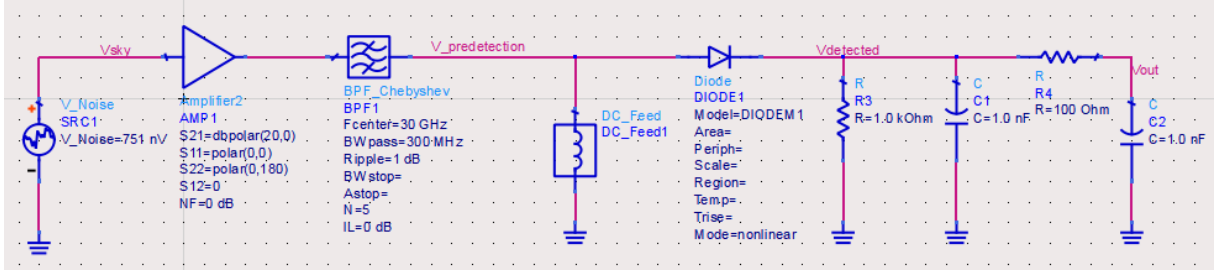


Figure 6.3: The circuit of the total power radiometer simulated in ADS RF/Microwave simulator.

The input signal represents the sky signal of the CMB radiation; for obtaining the voltage corresponding to the so-called V_{Noise} noise voltage source, the following steps have been followed taking into account that in RF literature the power is always defined with respect to an impedance of $Z_0 = 50 \text{ Ohm}$:

$$P_{sky} = k_B T_{sky} B = k_B (2.726\text{K}) B = 1.6566 \cdot 10^{-11} \text{ mWatt} \quad \rightarrow \quad v_{sky} = \sqrt{P_{sky} \cdot Z_0} \simeq 751 \text{ nV}. \quad (6.4)$$

Besides, the RF amplifier gain has been chosen to be 20 dB. The amplifier is an unilateral device because the scattering parameter S_{12} is null; what is more, as the S_{11} and S_{22} elements are also zero, we can ensure that its input and output impedances are adapted to the Z_0 impedance and so there will not be any loss in the amplification stage².

The bandpass filter chosen is a **Chebyshev prototype** one (in our case, of order 5) because this kind of filters provide a sharp attenuation in the stopband in return for a rippled passband response. As it can be seen in figure (6.3), it is in this filtering stage where we have defined the total power radiometer's detection bandwidth of 300 MHz.

The filtered signal is detected by a detector based on a Schottky diode and the detected signal suffers a further filtering carried out by a series RC filter. The Schottky diode is ideally defined in the RF/Microwave simulator and so in order to obtain consistent results we have had to set various parameters equal to the ones fixed in the data sheet from *Skyworks* attached to this work: we have chosen the values defined in Table 5 of such data sheet for the SMS7630 Series, where the values for saturation current, resistance, junction potential, etc are specified.

Once we have described the main characteristics of our circuit design, let's see which are the results obtained. In this first simulation, we have just the sky input signal and all other receiver components are ideal and do not add any noise to it. In this way, we will now simulate the output signal corresponding to this first ideal case in order to make sure that the radiometer response is acceptable and allows us to develop more complex analysis later on. We have represented the signals of our interest in the figures (6.4) and (6.5).

The effects of the different stages of the radiometer can easily be identified in figure (6.4).

Firstly, the red signal represents the sky input: as expected for a white noise contribution, its corresponding power spectrum is constant (we have plotted the $[n = 1]$ component of the signal, meaning that we are interested in the $f_0 = 30 \text{ GHz}$ component). Secondly, the predetection signal (blue coloured) belongs to the signal coming from the bandpass filter: as it can be seen, amplification has taken place and ripples appear in the passband signal. In this sense, it is interesting to point out the fact that we can even see

²For the case of unilateral amplifiers, the input and output reflection coefficients are equal to S_{11} and S_{22} respectively and so the fact that they are equal to zero means that there will not be any reflected wave going backwards.

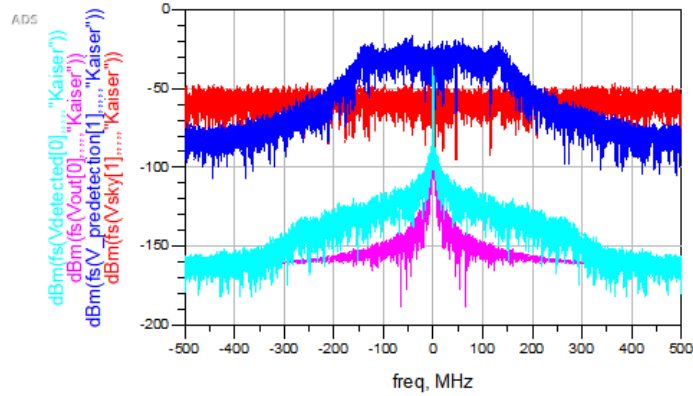


Figure 6.4: Power (in dBm units) spectra of the signal captured by the total power radiometer at its different stages. The red signal is the input sky signal; the blue signal is the predetection signal; the cyan signal is the detected one; the pink spectra corresponds to the last filtered output signal. In the vertical axis, the $[n]$ notation represents the order of the harmonic resulting from the TE simulation.

that the bandpass Chebyshev filter is of order 5: a total of precisely 5 peaks and valleys can be identified inside the passband for positive frequencies (0 – 300 MHz along the passband) and also for the respective negative ones (–300 – 0 MHz along the passband). Immediately after the filtering, the detector detects the RF power and provides it in the DC component of the cyan signal (note that in figure (6.4) the postdetection signals coming from the TE simulation are analysed around its DC component, i.e. the $[n = 0]$ harmonic). Finally, the detector smooths the detected signal: this low pass filtering can more clearly be observed in figure (6.5), where the small fluctuations are suppressed. It is also important to note that the detector does not collect all the RF power and provide it in the DC band; in figure (6.4), some losses can be identified comparing the blue (predetection) and the cyan and pink (postdetection) signals due to the diode’s performance (of course, in a real physical circuit losses would be higher).

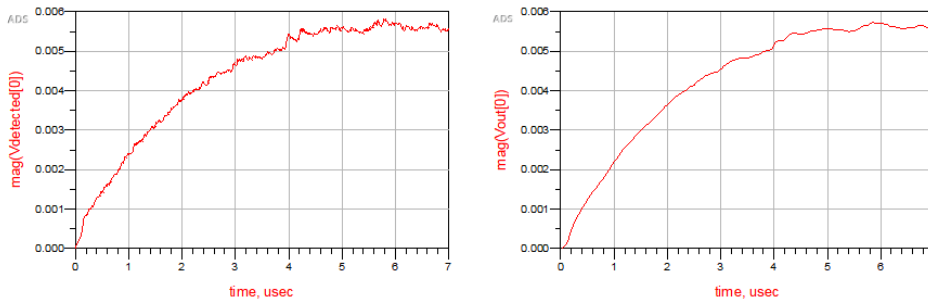


Figure 6.5: Postdetection signals: the left side signal is the one coming from the diode and the right side one represents the integrated smoother signal.

Taking into consideration these first results, it can be said that our design enables us to make a good qualitative interpretation of the total power radiometer’s role. We will now go one step beyond and **add the contribution of different noise sources**. On the one hand, we will introduce together with the sky signal an additional input signal representing the radiometer’s noise itself (the equivalent temperature of which being T_N , as in previous chapters). On the other, we will add the contribution of the amplifier’s gain variation too: we will generate a $1/f$ noise signal, which is going to be responsible for controlling the gain of the RF amplifier. The new circuit for the total power radiometer is rendered in figure (6.6).

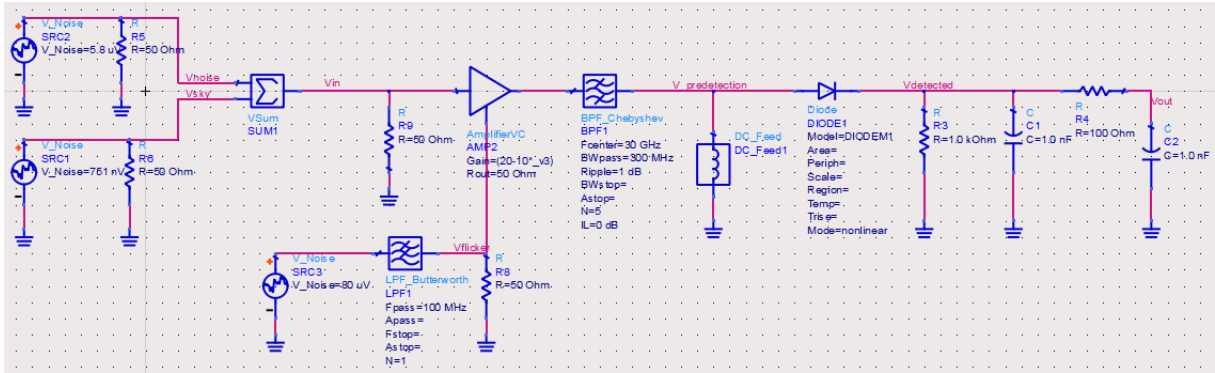


Figure 6.6: The new design of the total power radiometer: white noise characterising the receiver’s noise has been added, as well as the voltage controlled new amplifier.

Before analysing our results, we should make two important notes. First, when it comes to the receiver’s white noise contribution, we have considered an **equivalent noise temperature of $T_N = 160$ K**, as proposed in [13]. Thus, the voltage corresponding to this noise comes to be (following the same steps as in equation (6.4)) $\simeq 5.8 \mu\text{V}$; as we could have expected, it is indeed much bigger than that of the sky signal we are interested in and so this will clearly have a negative effect on our final results. And, second, the $1/f$ flicker noise contribution has been generated by proceeding to a **lowpass filtering of white noise**, as suggested in [2, 34]. The amplitude of the noise voltage in this case has been fixed to be the biggest one in all the circuit ($80 \mu\text{V}$) in order to get a distinguishable effect of the flicker noise by reaching an agreement between the corresponding knee frequency and the lowpass filter’s cutoff frequency.

As far as the circuit components are concerned, new blocks can be observed in picture (6.6). A voltage summer has been used in order to obtain the sum between the sky and the noise signal at the input of the radiometer, together with the corresponding resistors for impedance matching (the default input and output impedances of the voltage summer are, respectively, infinite and zero). Furthermore, the amplifier of figure (6.3) has been replaced by an ideal voltage-controlled RF amplifier: its gain follows the law $20\text{dB} - 10(\text{dB/V})v_{\text{flicker}}$ and, as a result, gain fluctuations will take place in our simulation. Finally, it could also be mentioned that the lowpass filter used for the generation of $1/f$ noise is a **Butterworth prototype** filter: we are now more interested in obtaining an adequate and realistic shape of the noise.

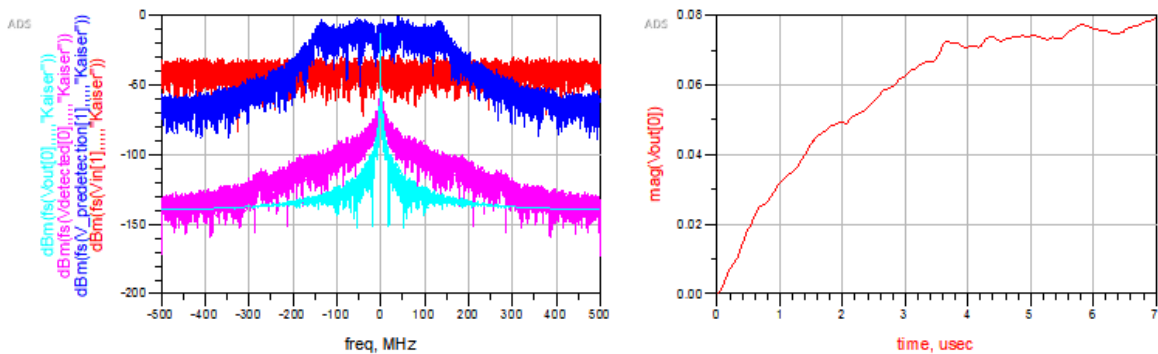


Figure 6.7: Results for the noisy total power radiometer. The left hand figure represents the power spectra at different stages and the right hand one the output integrated signal in time domain.

We have represented the results obtained in this second simulation in figure (6.7). The main features described in the previous simulation are once more present in this case (see left side figure). However, the noise contributions have led to rather different quantitative results. First of all, regarding the white noise contribution due to the receiver itself, it is evident that its effect has been to enhance each stage's signals' noise level (now we have got more dBm-s than in figure (6.4)).

Likewise, concerning the $1/f$ flicker noise, it must have had supplemented an extra noise contribution for frequencies below its knee frequency (f_{knee}). So as to see which the latter is, we must plot the radiometer's white noise spectra together with the flicker noise and see where both contributions are equal. We have shown this in figure (6.8).

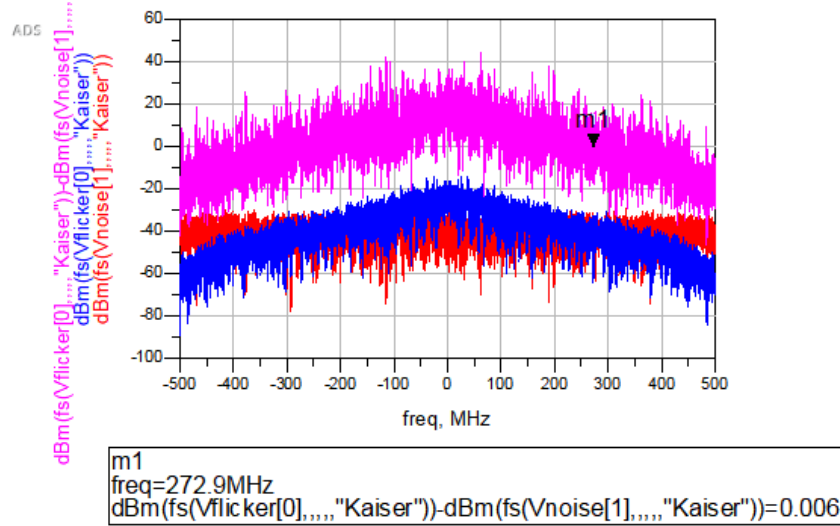


Figure 6.8: Determination of the knee frequency. The red signal represents the white noise contribution of the receiver, while the blue one is the flicker noise; the pink spectra is the difference between both of them.

The blue signal in the figure above makes it clear that we have obtained indeed a flicker noise signal by filtering white noise (we have had to choose a cutoff frequency of 100 MHz for the Butterworth filter, in order to get a good visual simultaneous representation of the flicker and white noises). In fact, the $m1$ point we have highlighted determines **the frequency at which the difference between the white noise and the flicker noise is nearly zero**: $f_{knee} \simeq 273$ MHz. Naturally, this value strongly differs from the Hz order of magnitude we should get at most in Planck Mission differential radiometers, but bear in mind that we have intentionally manipulated noise values so as to make it possible to study and visualize the different effects we have analytically explained in the previous chapters.

Hence, it is obvious that the two new noise signals we have added in this second simulation absolutely hide our sky signal of interest. This can be seen in figure (6.7), where the output signal's order of magnitude has been enhanced by a factor of 10 and so we have no chance to discover where the CMB signal might lie down there.

Ergo we have no other option but to study the performance of the pseudo-correlation radiometer and see whether it is indeed a more profitable and adequate choice for the measurement of radio astronomic signals as the CMB radiation.

6.2.2 Pseudo-correlation radiometer simulation

In the case of the differential or pseudo-correlation radiometer, we are going to follow the same steps as for the total power radiometer. We will first carry out a simulation with just our input signal of interest (no noise) and see whether the radiometer’s response is appropriate or not. After that, we will study the performance of the radiometer with the presence of both white and flicker noise, the former being a characterisation of the receiver’s noise and the latter coming from the gain imbalance between both radiometric branches. We present our first pseudo-correlation radiometer design in the following figure (6.9).

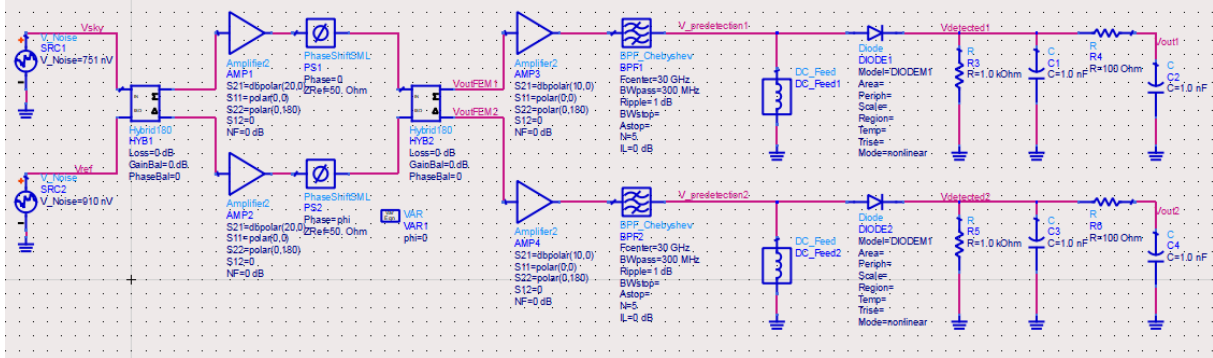


Figure 6.9: Ideal pseudo-correlation radiometer design. The phase shift of the second branch’s switcher has been defined as a sweep parameter in order to be able to simulate both switch states.

As it can be observed, the BEMs of the radiometer are analogous to the total power radiometer designed in figure (6.3). With respect to the FEMs, two new components have been used: the 180° -hybrids, responsible for the coupling of the two branches’ signals, and the phase shifters. Moreover, the input signal of the first branch is the sky signal, while the second branch’s input now turns out to be the one that corresponds to the **4 K reference load** (in this case, the voltage takes a value of ≈ 910 nV).

With the aim of ensuring the desirable performance, as the BEMs’ have already been tested in the total power radiometer simulations, we should study the FEMs’ proper execution. For doing so, we can for instance plot the radiometer’s output signals and see whether in each switch state the sky and reference signals are alternated between both branches. As defined in the analytical model of chapter 5, the first branch will add no phase shift, whereas we have defined as a sweep variable the phase introduced by the second branch’s shifter. Hence, we plot the results in figure (6.10).

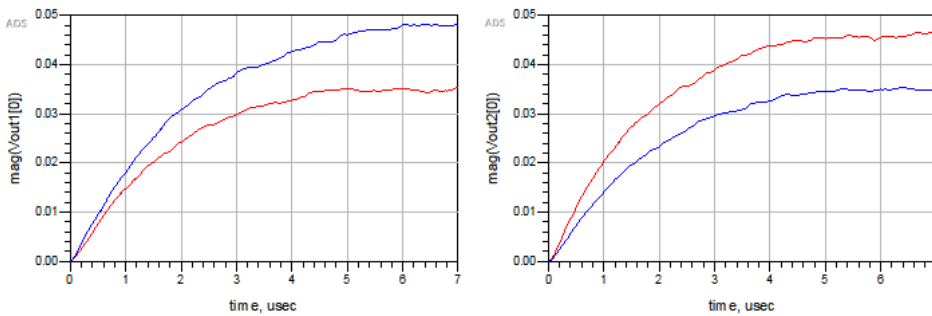


Figure 6.10: The output signals of the first radiometric branch (left) and the second one (right). The red signals represent the $\theta_1 = 0$ phase state, while the blue ones correspond to the $\theta_2 = \pi$ state.

As the analytical model we have developed in chapter 5 predicts, in the first switch state where $\theta_1 = 0$, the output at the first branch is proportional to the weaker sky signal (remember that $T_{sky} = 2.726$ K and $T_{ref} = 4$ K) and the lower second branch's output is proportional to the reference load. Whereas when the lower phase shifter introduces a phase shift of π in the second arm, **the branches exchange their output signals**.

Let's now see which is the performance of the pseudo-correlation radiometer we have designed in ADS simulator with respect to noise addition. In this spirit, we are going to follow **the same strategy as in the case of the total power radiometer**: white noise will be added at the input ports for the characterisation of receiver's noise and a voltage-controlled amplifier will be used for the introduction of gain fluctuations.

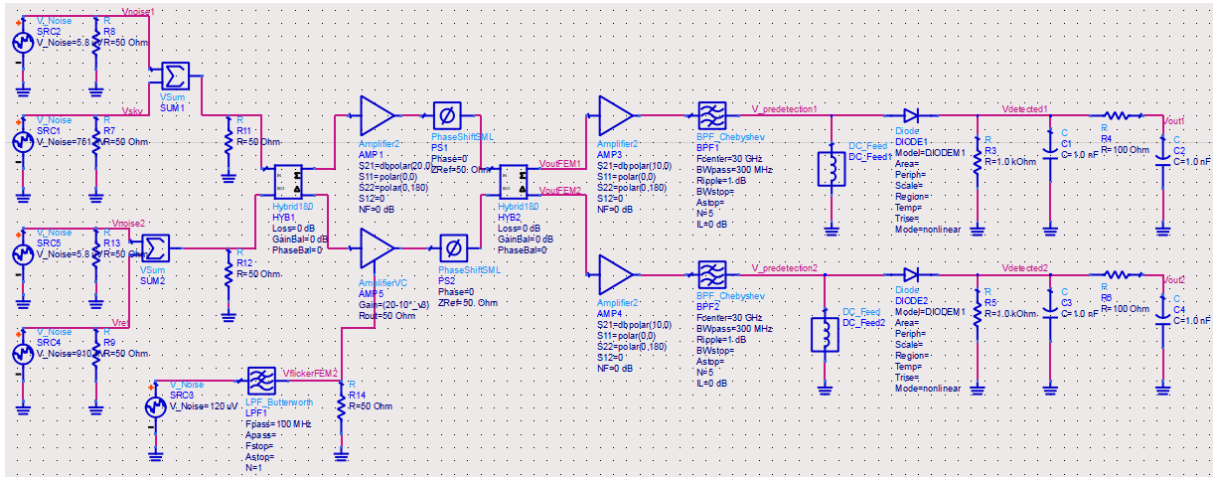


Figure 6.11: The output signals of the first radiometric branch (left) and the second one (right). The red signals represent the $\theta_1 = 0$ phase state, while the blue ones correspond to the $\theta_2 = \pi$ state.

The situation we have proposed is the one of the figure (6.11): it is the FE-amplifier of the second branch the one that will present gain variations and both inputs will simultaneously present additive white noise contributions. In this way, we will in the following analyse how signals change in this case, study the advantages provided by the pseudo-correlation radiometer compared to the total power one, and see the importance of the gain modulation factor technique developed in Planck Mission.

So as to do so, we will consider a **fixed phase-switch state** from now on: we will fix $\theta_1 = 0$ and so we know that the output signal up in the first branch will belong to the sky input and that in the second branch to the reference input. Let's first take a look to the output DC voltages we obtain in both branches once the simulation has been run (see figure (6.12)). In this case, it can be observed that due to the high noise contributions both outputs are almost equal and indistinguishable (there must be a small difference because the reference signal is just a little higher than the sky one, but in the scales of the noise signals the mentioned difference turns out to be ridiculous).

Unlike the total power radiometer, **we are now in a more advantageous position because we do know that sky and reference signals have been altered in an exactly same way** and, as it is known that the reference load temperature corresponds to $T_{ref} = 4$ K, we can also get to know the ideal output DC voltage we should obtain in the case of a noise-free reference signal. Hence, from the right hand figure of (6.11) **the total contribution of noise could be extracted** and, consequently, from the left hand figure of (6.11) the temperature of the (in theory) unknown CMB could be measured.

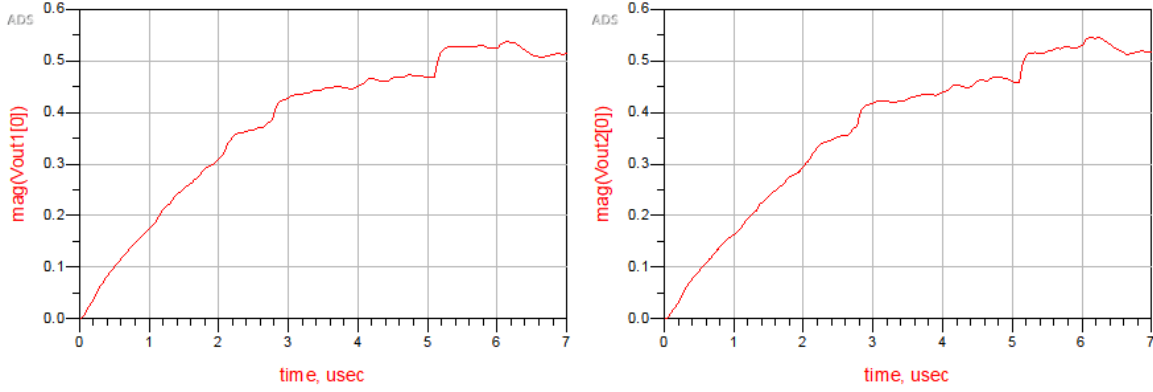


Figure 6.12: The output signals of the first (left) and second (right) branches for a noisy pseudo-correlation radiometer.

Although it could quite easily be done, it is beyond the scope of this section's main goal to introduce ourselves in such numerical calculations.

What we have just explained was already known from the Planck Mission description carried out in previous sections. It is now a good point to study **the effect of the gain modulation factor (r) multiplication and the subsequent differentiation** of the branches' signals. According to our analytical model of chapter 5, the proper value of r would be the following one in our simulations:

$$r = r_0 = \frac{T_{sky} + T_N}{T_{ref} + T_N} = \frac{2.726 \text{ K} + 160 \text{ K}}{4 \text{ K} + 160 \text{ K}} = 0.992231707. \quad (6.5)$$

Knowing this value, we will now see whether the $v_{sky} - r_0 \cdot v_{ref}$ signal vanishes (remember that in the considered phase switch state the sky signal is located in the upper first branch and the reference one in the lower second branch). We have plotted this difference in the following figure (6.13).

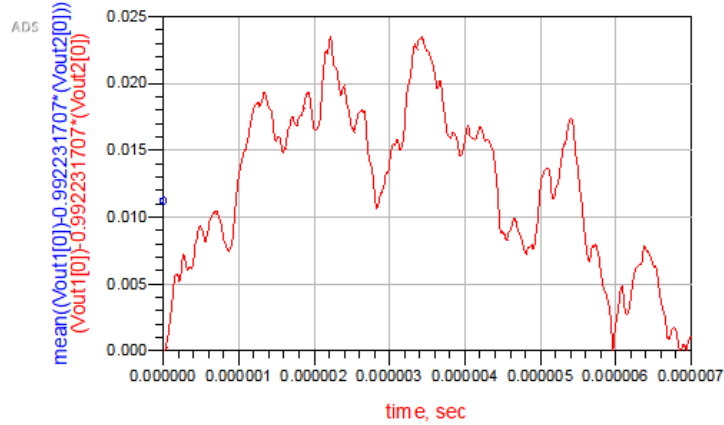


Figure 6.13: The signal proportional to the reference load has been multiplied by the proper $r = r_0$ value and the difference of the signal proportional to the sky input with it has been plotted. The mean value has been marked by a small blue spot in the vertical axes: ≈ 0.011 .

As expected, the resulting signal comes to be relatively close to zero (the mean in the 7 μsec simulation stop time has been of ≈ 0.011). Of course, we could have obtained a better result by making much more

measurements and taking the average value of them or, moreover, other switch states could have also been considered and see a more noticeable signal suppression. In order to enforce the idea of the preferred $r = r_0$ gain modulation value, we will study a last effect. Remember that, as we saw in the last sections of chapter 5, the **gain fluctuations' flicker noise corresponding to the FE-amplifiers should also be removed with $r = r_0$** . Voilà the reason for considering gain variations of the second branch's FE-amplifier in figure (6.11): having designed this particular situation will enable us to strengthen the importance of a good choice of r and analyse the effect on our signals' spectra.

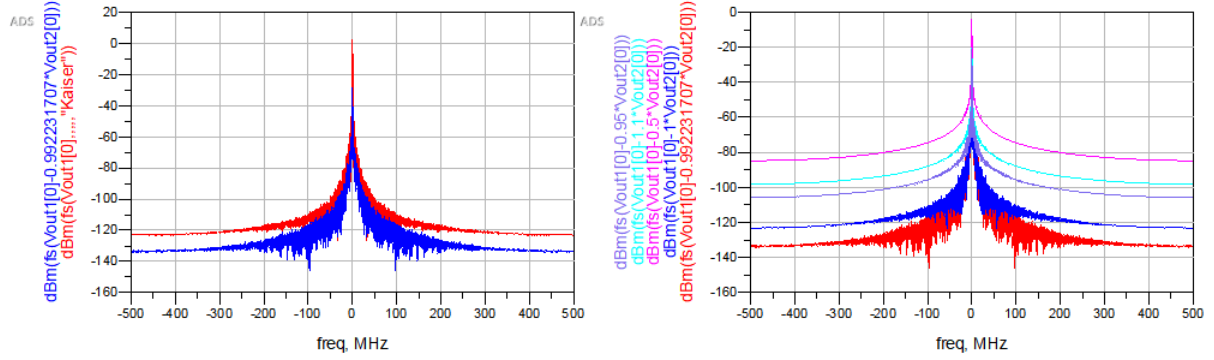


Figure 6.14: The left hand figure shows the comparison between the power spectrum of the first branch's output DC signal (red curve) and the spectrum corresponding to $v_{sky} - r_0 \cdot v_{ref}$ (blue curve). In the right hand figure the latter has been plotted for different values of r .

Two important ideas can be concluded for the results obtained and represented in figure (6.14):

- The left hand plot shows not only that the overall noise contribution is decreased, but it can also be observed that particularly the $1/f$ noise presence is reduced: the width of the spectrum is narrower in the case of the r -multiplied and differentiated signal (blue curve) than in the case of the output DC signal proportional to the sky input alone (red curve).
- As for the right hand graphic, another very relevant result has been achieved. We have plotted the power spectrum of the $v_{sky} - r \cdot v_{ref}$ signal for different values of r (most of them near r_0) and, as we must have expected, the maximum suppression of noise has been obtained for the choice of $r = r_0 = 0.992231707$ (red spectrum). Other r choices lead to a higher noise presence (the more the value is distanced from r_0 , the weaker the noise abolition is).

Multiple simulations have been carried out and almost all of them have led to the described results. As a consequence, we have been able to see the great importance of the proper gain modulation factor choice, as well as **the rather advantageous and suitable measurement method behind the pseudo-correlation radiometer used in Planck Mission**.

However, it is fair to say that our simulations are valid so as to make a quite qualitative study of the radiometers and their signals. Above all, it should not be forgotten the fact that we have been dealing with system-level simulations and that the values of different parameters and components have been fixed to fit our simulation requirements, though they differ from real-design values.

Chapter 7

Conclusions and outlook

Taking into account all we have said in the previous sections, we can reach several conclusions. It is evident that the CMB radiation can be understood as a photography of the early Universe, taken 380000 years after the Hot Big Bang singularity. Bearing in mind that Universe keeps expanding, this radiation comes to be so weak that radio astronomers have had to deal with really demanding projects. In this spirit, the alternative presented by Dicke did suppose an innovative change of perspective in terms of radio signals' detection. Indeed, Dicke's switching idea can be considered as the precedent of the correlation radiometer and, consequently, also as the fundamental basis laying on the differential radiometer used in Planck Mission.

Therefore, we have been able to study the different units conforming the Planck Low Frequency Instrument: the electromagnetic design of the antennas and the OMTs can help us to understand why the Planck LFI radiometers have been so successful for instance in the CMB polarisation measurement. Furthermore, the RF circuitry employed in Planck radio receivers does suppose a quite interesting insight of the performance of high frequency electronic systems.

Appart from that, the development of the analytical model has provided a mathematical tool for understanding and proving the results obtained in Planck Mission. What is more, the RF/Microwave simulator from ADS software has reinforced our theoretical predictions. In this way, it should be said that the fact of being working with such weak and noisy signals has supposed a major difficulty for both obtaining physically meaningful results and making the appropriate interpretations. However, we have been able to prove that our system- or block-level designs have been enough and very useful for, at least, making a qualitative study of the functionality of the total power radiometer and the pseudo-correlation radiometer.

In fact, this final degree project can be continued by, for example, making more detailed designs of the circuits we have analysed and in that way obtain more exact and precise numerical results. Other tools such as Simulink or Matlab could be of great aid in this sense. In addition, keep in mind that in this work we have focused on the measurement of the CMB temperature; future work could also consist of analysing the basis of the CMB polarisation (Stokes parameters, etc) and study the instrumentation needed for such measurements: the so-called polarimeters.

It is clear that cosmology and radiometry are two scientific fields that are tightly connected and they feed one each other. As such knowledge areas are constantly going under new uncertainties, it is obvious that many other new missions are being designed for constraining them and answering the open questions that have not still been clarified. These are one of the most attractive and challenging projects that are being carried out nowadays and other that will be held in the following years:

- The **QUIJOTE** Experiment: this ground experiment is already operating thanks to the collaboration work of the Instituto de Astrofísica de Canarias, the Instituto de Física de Cantabria, the Departamento de Ingeniería de Comunicaciones of Universidad de Cantabria, University of Cambridge, University of Manchester and Idom Company. This project was started in November 2012, and its main objectives are to detect B-modes induced by gravitational waves and to collect information about the polarisation of foreground emissions at low frequencies (10-40 GHz) [6]. The project consists of two telescopes located in the Teide Observatory of Canary Islands (Spain), which include three instruments: the Multi-Frequency Instrument (covering the frequency range of 10-20 GHz), the 30-GHz Instrument and the 40-GHz Instrument. The first instrument contains a total of 32 channels, while each of the last two instruments contain 31 polarimeters working at their respective frequencies. All the information provided by them will suppose an extra supplement for Planck results.
- The **GroundBIRD** Project: this is another ground telescope experiment, resulting from the collaboration among the Instituto de Física de Canarias and other scientific teams from Japan, Korea and The Netherlands. A high speed (20 rpm \simeq 120°/s) scanning will be used in GroundBIRD in order to minimise the $1/f$ noise contribution coming from the atmosphere and from the instrument itself. The telescope will contain a total number of 450 cooled microwave kinetic inductance detectors (MKIDs), working at two channels of 145 GHz and 220 GHz [4]; additionally, the groundBIRD project's main goal will be to provide extra data about the CMB polarisation. The telescope is planned to be deployed at the Teide Observatory by summer of this year 2019.
- The **LiteBIRD** Project: this space experiment is planned to be launched in 2027 by the Japan Aerospace Exploration Agency (JAXA). The LiteBIRD has special similarities with Planck Mission [4]: it has been designed to contain two instruments (The High and The Low Frequency Telescopes), it will be orbiting at the Lagrangian L2 point of the Earth-Sun system and will provide full-sky information about the $l = 2 - 200$ temperature and polarisation multipoles. The observed frequencies will cover a spectral response from 34 GHz to 448 GHz, and more than 3000 bolometers will be used for CMB detection [23].

Thus, we can say that there is still a lot of work to be done in this fascinating area and that we may someday be able to clear up the hole history of our Universe and, why not, the intriguing future that awaits us all.

References

- [1] Juan Maria Aguirregabiria Aguirre. *Grabitazioa eta Kosmologia*. Universidad del Pais Vasco/Euskal Herriko Unibertsitatea.
- [2] Beatriz Aja Abelán. *Amplificadores de banda ancha y bajo ruido basados en tecnología de GaAs para aplicaciones de radiometría [PhD thesis]*. Universidad de Cantabria, 2007.
- [3] Y Akrami et al. “Planck 2018 results. I. Overview and the cosmological legacy of Planck”. In: *arXiv preprint arXiv:1807.06205* (2018).
- [4] C. Baccigalupi et al. “European Cosmic Microwave Background Studies: Context and Roadmap”. In: (2018).
- [5] Unai Arregi Leon. “Planck Sateliteak Behatutako Fisika: Mikrouhin Erradiazio Kosmikoaren (CMB) Temperatura Anisotropien Azterketa”. In: (2019).
- [6] Instituto de Astrofísica de Canarias. *Anisotropy of the Cosmic Microwave Background*. URL: <http://www.iac.es/proyecto/cmb/pages/en/home-cmb.php>.
- [7] Daniel Baumann. “Cosmology, part III mathematical tripos”. In: *University lecture notes* (2014).
- [8] M Bersanelli and N Mandolesi. “Design concept of the Planck-LFI instrument”. In: *Astrophysical Letters and Communications* 37 (2000), p. 171.
- [9] Marco Bersanelli et al. “Planck pre-launch status: Design and description of the Low Frequency Instrument”. In: *Astronomy & Astrophysics* 520 (2010), A4.
- [10] Artem Boriskin and Ronan Sauleau. *Aperture Antennas for Millimeter and Sub-Millimeter Wave Applications*. Springer, 2018.
- [11] Graham Brooker. *Introduction to sensors for ranging and imaging*. The Institution of Engineering and Technology, 2009.
- [12] Martin Bucher. “Physics of the cosmic microwave background anisotropy”. In: *International Journal of Modern Physics D* 24.02 (2015), p. 1530004.
- [13] Yali Chen, Yonghong Zhang, and Yong Fan. “Simulation model of the wideband total power radiometer”. In: *2010 International Symposium on Intelligent Signal Processing and Communication Systems*. IEEE. 2010, pp. 1–4.
- [14] “Circuit Envelope Simulation”. In: *Agilent Technologies* (2006).
- [15] J. M. D. Coey. “Lecture 3: Signal and Noise”. In: *School of Physics and CRANN, Trinity College Dublin (Ireland)* ().
- [16] Planck Collaboration Collaboration et al. “Planck Blue Book”. In: *ESA Planck blue book, ESA* (2005).
- [17] Francesco Cuttaia et al. “Planck-LFI radiometers tuning”. In: *Journal of Instrumentation* 4.12 (2009), T12013.
- [18] O D’Arcangelo et al. “The Planck-LFI flight model composite waveguides”. In: *Journal of Instrumentation* 4.12 (2009), T12007.

- [19] O D’Arcangelo et al. “The Planck-LFI flight model ortho-mode transducers”. In: *Journal of Instrumentation* 4.12 (2009), T12005.
- [20] European Space Agency (ESA). *planck*. URL: <http://sci.esa.int/planck/>.
- [21] DJ Fixsen. “The temperature of the cosmic microwave background”. In: *The Astrophysical Journal* 707.2 (2009), p. 916.
- [22] JM Herreros et al. “The Planck-LFI radiometer electronics box assembly”. In: *Journal of Instrumentation* 4.12 (2009), T12008.
- [23] JAXA. *LiteBIRD. Lite (Light) satellite for the studies of B-mode polarization and Inflation from cosmic background Radiation Detection*. URL: <http://litebird.jp/eng/>.
- [24] John D Kraus. “Radio astronomy”. In: *New York: McGraw-Hill, 1966* (1966).
- [25] J-M Lamarre et al. “Planck pre-launch status: The HFI instrument, from specification to actual performance”. In: *Astronomy & Astrophysics* 520 (2010), A9.
- [26] Hans-Dieter Lang and Xingqi Zhang. “The Harmonic Balance Method (ECE 1254 project report)”. In: *Modeling of multiphysics systems* 5 (2013), p. 10.
- [27] Andrew Liddle. *An introduction to modern cosmology*. John Wiley & Sons, 2015.
- [28] A Mennella et al. “The linearity response of the Planck-LFI flight model receivers”. In: *Journal of Instrumentation* 4.12 (2009), T12011.
- [29] G Morgante et al. “Cryogenic characterization of the Planck sorption cooler system flight model”. In: *Journal of Instrumentation* 4.12 (2009), T12016.
- [30] Viatcheslav Mukhanov. *Physical foundations of cosmology*. Cambridge university press, 2005.
- [31] NASA. *NASA on The Commons*. URL: <https://www.flickr.com/photos/nasacommons>.
- [32] Alan V Oppenheim, Alan S Willsky, and S Hamid Nawab. *Señales y sistemas*. Pearson Educación, 1998.
- [33] Robert B Partridge. *3K: the cosmic microwave background radiation*. Cambridge University Press, 1995.
- [34] JP Pascual et al. “System simulation of a differential radiometer using standard RF-microwave simulators”. In: *Simulation* 81.11 (2005), pp. 735–755.
- [35] Guido Walter Pettinari. “The intrinsic bispectrum of the Cosmic Microwave Background [PhD thesis]”. In: *arXiv preprint arXiv:1405.2280* (2014).
- [36] Joaquín Portilla Rubín. *Sistemas de Comunicación*. Universidad de Cantabria (Curso de Verano).
- [37] David M Pozar. *Microwave Engineering*. JohnWiley & Sons, 1998.
- [38] Kristen Rohlfis and Thomas L Wilson. *Tools of radio astronomy*. Springer Science & Business Media, 1996.
- [39] Matts Roos. *Introduction to cosmology*. John Wiley & Sons, 2015.
- [40] Michael Seiffert et al. “ $1/f$ noise and other systematic effects in the Planck-LFI radiometers”. In: *Astronomy & Astrophysics* 391.3 (2002), pp. 1185–1197.
- [41] Niels Skou and David M Le Vine. *Microwave Radiometer Systems. Design and Analysis*. Artech House, 2006.
- [42] Jan Alexander Tauber et al. “Planck pre-launch status: The Planck mission”. In: *Astronomy & Astrophysics* 520 (2010), A1.
- [43] ME Tiuri. “Radio astronomy receivers”. In: *IEEE Transactions on Military Electronics* 8.3 (1964), pp. 264–272.
- [44] Fabrizio Villa et al. “High performance corrugated feed horns for space applications at millimetre wavelengths”. In: *Experimental Astronomy* 14.1 (2002), pp. 1–15.

- [45] Fabrizio Villa et al. “Planck pre-launch status: Calibration of the Low Frequency Instrument flight model radiometers”. In: *Astronomy & Astrophysics* 520 (2010), A6.
- [46] F Villa et al. “Planck-LFI flight model feed horns”. In: *Journal of Instrumentation* 4.12 (2009), T12004.
- [47] David F Wait. “The sensitivity of the Dicke radiometer”. In: *J. Res. Natl. Bur. Stand* 71.2 (1967), pp. 127–152.
- [48] Keqian Zhang et al. *Electromagnetic theory for microwaves and optoelectronics*. Springer, 2008.
- [49] Andrea Zonca. *Advanced modelling and combined data analysis of Planck focal plane instruments [PhD thesis]*. Università degli Studi di Milano and Université Paris Diderot, 2009.

DATA SHEET

Surface-Mount Mixer and Detector Schottky Diodes

Applications

- Sensitive RF and microwave detector circuits
- Sampling and mixer circuits
- High-volume wireless
- Wi-Fi and mobile
- Low-noise receivers in high-sensitivity ID tags
- Radio designs

Features

- Tight parameter distribution
- Available as singles, pairs, and dual pairs
- Packages rated MSL1, 260 °C per JEDEC J-STD-020



Skyworks Green™ products are compliant with all applicable legislation and are halogen-free. For additional information, refer to *Skyworks Definition of Green™*, document number SQ04-0074.




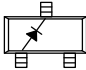
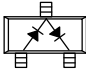
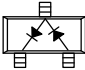
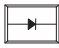
Description

These low-cost, surface-mountable, plastic-packaged silicon mixer Schottky diodes are designed for RF and microwave mixers and detectors. They include low-barrier diodes and zero-bias detectors that combine Skyworks advanced semiconductor technology with low-cost packaging techniques. All diodes are 100 percent DC tested and deliver tight parameter distribution, which minimizes performance variability.

These diodes are available in SOD-882, SC-79, and SOT-23 packages. Wiring configurations include singles, series pairs, and reverse series pairs. They may be used at frequencies up to 24 GHz.

Table 1 describes the various packages and marking of the mixer and detector Schottky diodes.

Table 1. Schottky Diode Packaging and Marking

				
Single	Single	Series Pair	Reverse Series Pair	Single
SC-79 Green™	SOT-23	SOT-23	SOT-23	SOD-882 Green™
◆ SMS7621-079LF Marking: Cathode and SA	SMS7621-001LF Green™ Marking: XH1	◆ SMS7621-005LF Green™ Marking: XH2	◆ SMS7621-006LF Green™ Marking: XH8	SMS7621-040LF Marking: E
◆ SMS7630-079LF Marking: Anode and SC		SMS7630-005LF Green™ Marking: XD2	◆ SMS7630-006LF Green™ Marking: XD8	SMS7630-040LF Marking: P
$L_S = 0.7 \text{ nH}$	$L_S = 1.5 \text{ nH}$	$L_S = 1.5 \text{ nH}$	$L_S = 1.5 \text{ nH}$	$L_S = 0.45 \text{ nH}$

Electrical and Mechanical Specifications

The absolute maximum ratings of the mixer and detector Schottky diodes are provided in Table 2. Electrical specifications are provided in Tables 3 and 4. The associated SPICE model parameters are provided in Table 5. A typical detector schematic diagram is shown in Figure 1.

Typical performance characteristics are illustrated in Figures 2 and 3. Package dimensions are shown in Figures 4 to 8 (even numbers), and tape and reel dimensions are provided in Figures 5 to 9 (odd numbers).

Package and Handling Information

Instructions on the shipping container label regarding exposure to moisture after the container seal is broken must be followed. Otherwise, problems related to moisture absorption may occur when the part is subjected to high temperature during solder assembly.

The mixer and detector Schottky diodes are rated to Moisture Sensitivity Level 1 (MSL1) at 260 °C for 5 seconds. They can be used for lead or lead-free soldering. For additional information, refer to the Skyworks Application Note, *Solder Reflow Information*, document number 200164.

Care must be taken when attaching this product, whether it is done manually or in a production solder reflow environment. Production quantities of this product are shipped in a standard tape and reel format.

Table 2. Absolute Maximum Ratings¹

Parameter	Symbol	Minimum	Maximum	Units
Reverse voltage	V_R		Rated V_B	V
Forward current, steady state	I_F		50	mA
Power dissipation	P_D		75	mW
Storage temperature	T_{STG}	-65	+150	°C
Operating temperature	T_A	-65	+150	°C
Junction temperature	T_J		+150	°C

¹ Exposure to maximum rating conditions for extended periods may reduce device reliability. There is no damage to device with only one parameter set at the limit and all other parameters set at or below their nominal value. Exceeding any of the limits listed here may result in permanent damage to the device.

ESD HANDLING: *Although this device is designed to be as robust as possible, electrostatic discharge (ESD) can damage this device. This device must be protected at all times from ESD when handling or transporting. Static charges may easily produce potentials of several kilovolts on the human body or equipment, which can discharge without detection. Industry-standard ESD handling precautions should be used at all times.*

Table 3. Electrical Specifications¹

($T_A = +25$ °C Per Junction, Unless Otherwise Noted)

Part Number	Barrier	Minimum V_B @ 10 μ A (V)	Typical C_T @ 0 V (pF)	V_F @ 1 mA (mV)	Maximum Pair Configuration ΔV_F @ 1 mA (mV)	Maximum R_T ² (Ω)
SMS7621 series	Low	2	0.25	260 to 320	10	18 @ 5 mA

¹ Performance is guaranteed only under the conditions listed in this table.

² R_T is the slope resistance.

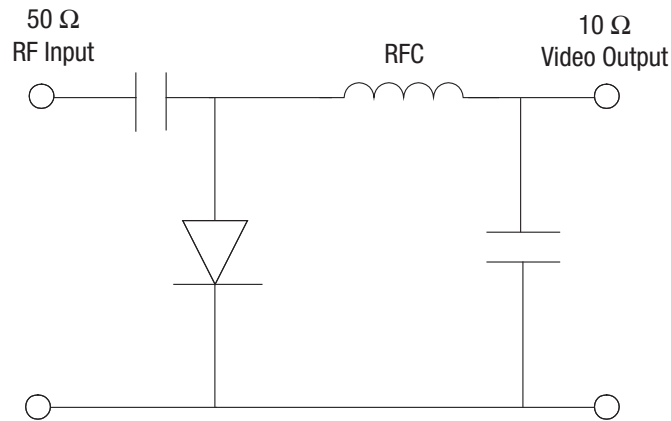
Table 4. Electrical Specifications¹
(T_A = +25 °C Per Junction, Unless Otherwise Noted)

Part Number	Minimum V _b @ 100 μA (V)	Typical C _T @ 0.15 V (pF)	V _F @ 0.1 mA (mV)	V _F @ 1 mA (mV)	Maximum Pair Configuration ΔV _F @ 1 mA (mV)	Typical R _v (Ω)
SMS7630 series	1	0.3	60 to 120	135 to 240	10	5000

¹ Performance is guaranteed only under the conditions listed in this table.

Table 5. SPICE Model Parameters (Per Junction)

Parameter	Units	SMS7621 Series	SMS7630 Series
I _s	A	4E-8	5E-6
R _s	Ω	12	20
N	-	1.05	1.05
TT	sec	1E-11	1E-11
C _{JO}	pF	0.1	0.14
M	-	0.35	0.40
E _g	eV	0.69	0.69
X _{TI}	-	2	2
F _c	-	0.5	0.5
B _v	V	3	2
I _{bv}	A	1E-5	1E-4
V _J	V	0.51	0.34



200041-001

Figure 1. Typical Detector Circuit

Typical Performance Characteristics

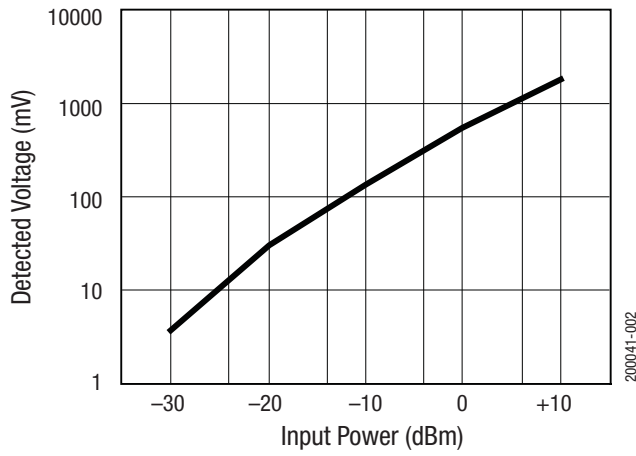


Figure 2. Typical Detector Characteristics @ 1.8 GHz

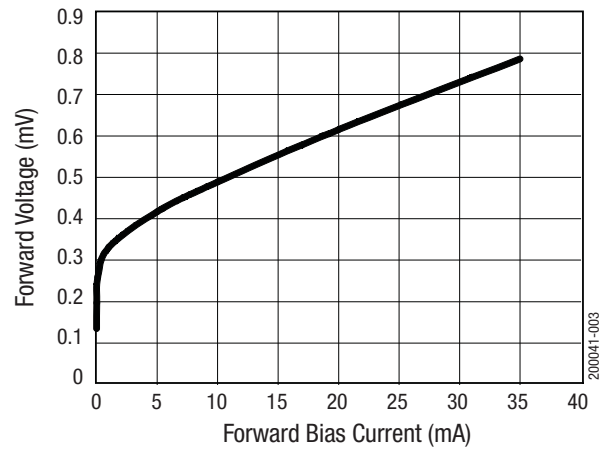
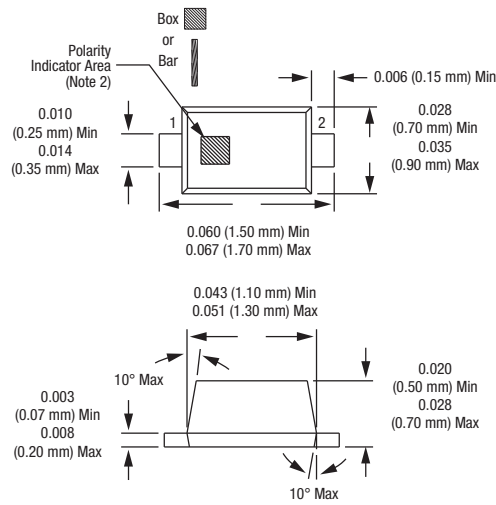


Figure 3. SMS7621 Forward Voltage vs Forward Bias Current

DATA SHEET • MIXER AND DETECTOR SCHOTTKY DIODES

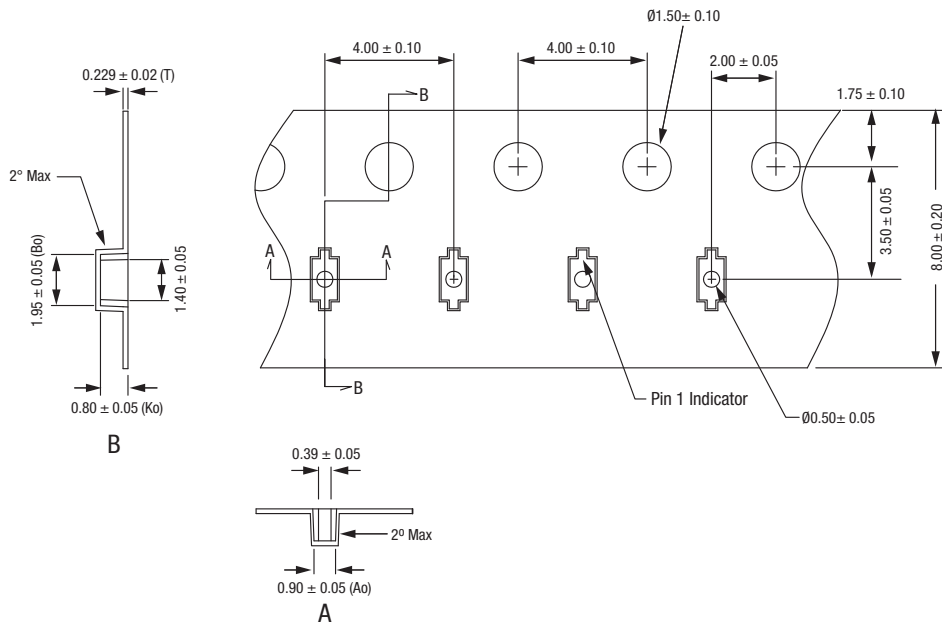


Notes:

1. Dimensions are in inches (millimeters shown in parentheses).
2. Cathode indicator for SMS7621-079LF
Anode indicator for SMS7630-079LF

200041-006

Figure 4. SC-79 Package Dimension Drawing

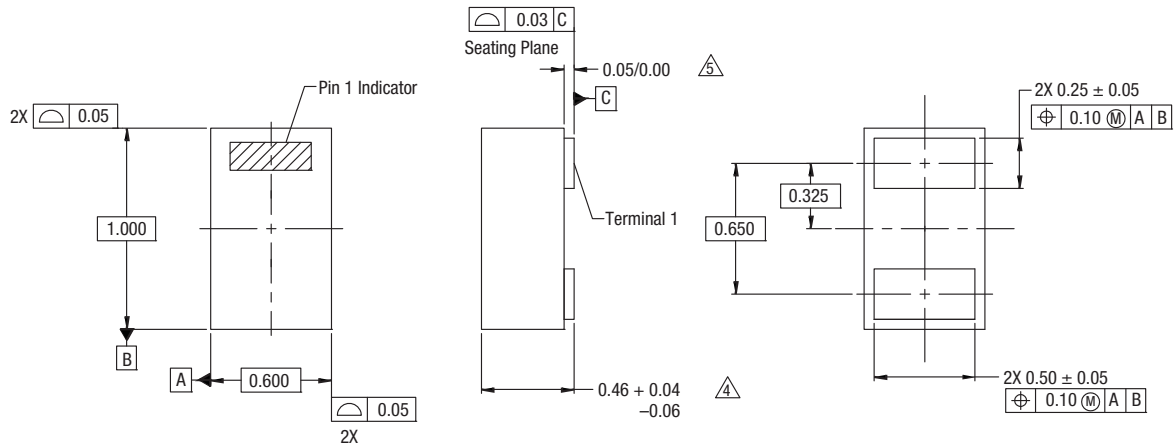


Notes:

1. Carrier tape: black conductive polycarbonate or polystyrene.
2. Cover tape material: transparent conductive PSA.
3. Cover tape size: 5.4 mm width.
4. ESD-surface resistivity is $\leq 1 \times 10^8$ Ohms/square per EIA, JEDEC TNR Specification.
5. All measurements are in millimeters.

200041-007

Figure 5. SC-79 Tape and Reel Dimensions

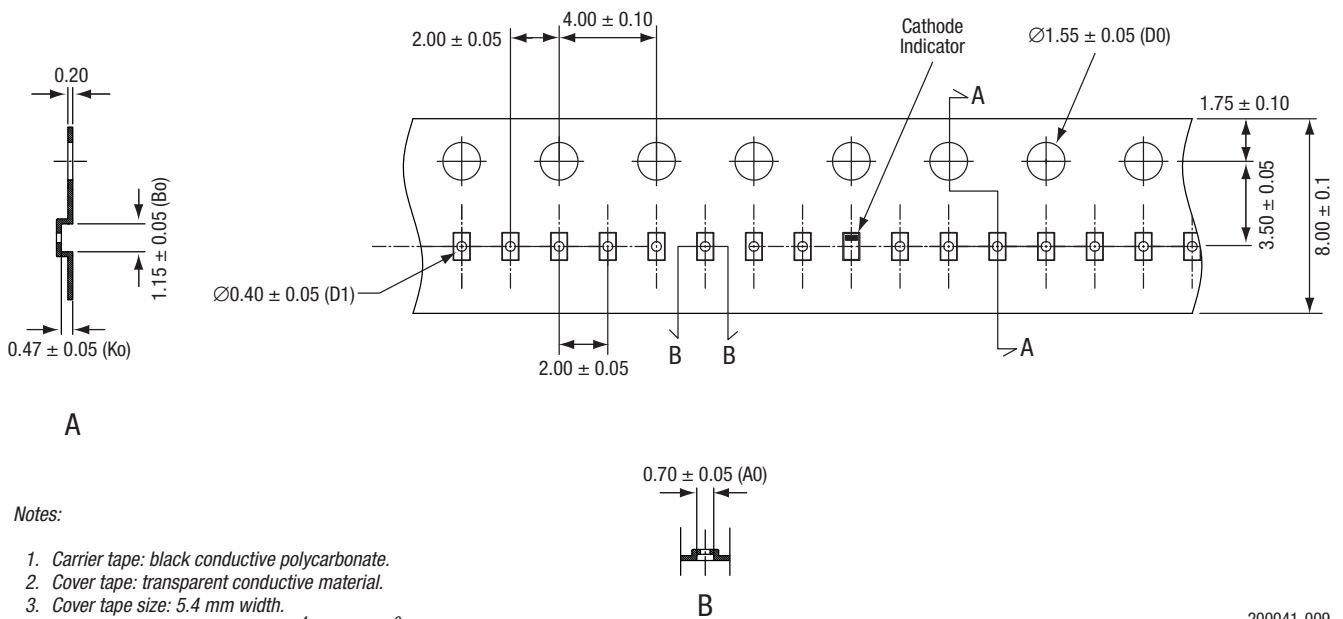


Notes:

1. All measurements are in millimeters.
2. Dimensions and tolerances according to ASME Y14.5M-1994.
3. These packages are used principally for discrete devices.
4. This dimension includes stand-off height and package body thickness, but does not include attached features, e.g., external heatsink or chip capacitors. An integral heatslug is not considered an attached feature.
5. This dimension is primarily terminal plating, but does not include small metal protrusion.

200041-008

Figure 6. SOD-882 Package Dimension Drawing



Notes:

1. Carrier tape: black conductive polycarbonate.
2. Cover tape: transparent conductive material.
3. Cover tape size: 5.4 mm width.
4. ESD surface resistivity is $\geq 1 \times 10^4 \sim \leq 1 \times 10^8$ Ohms/square.
5. All dimensions are in millimeters.

200041-009

Figure 7. SOD-882 Tape and Reel Dimensions

DATA SHEET • MIXER AND DETECTOR SCHOTTKY DIODES

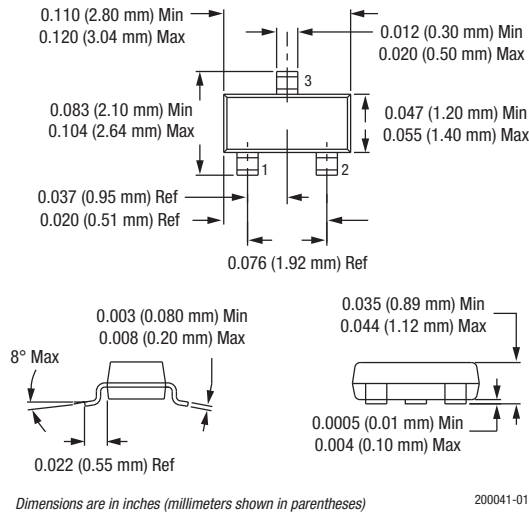
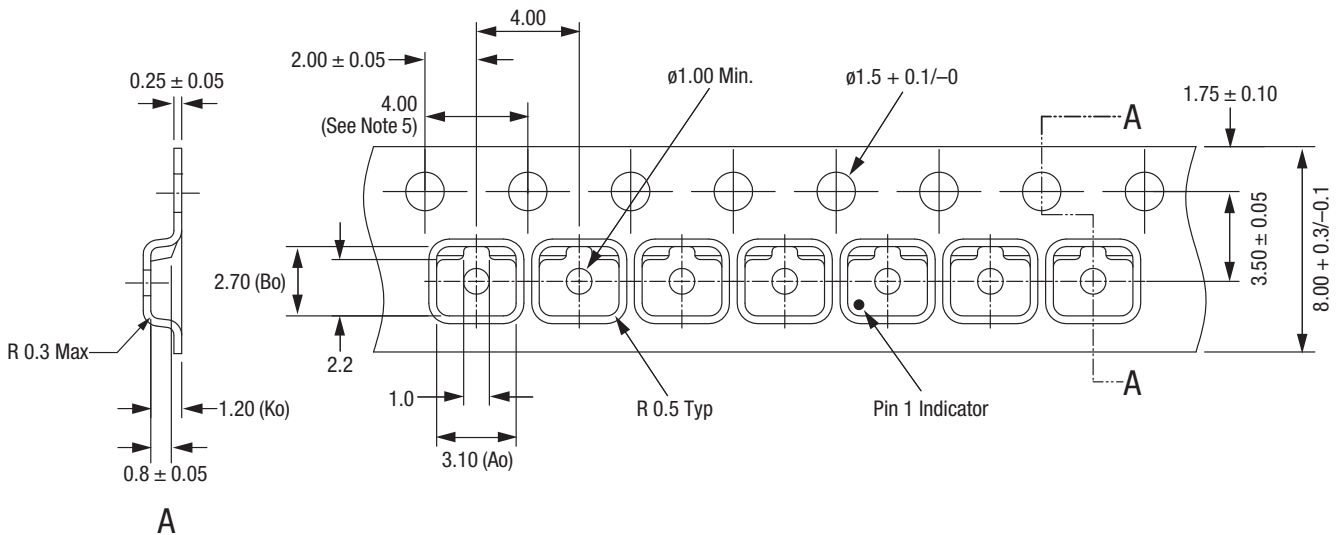


Figure 8. SOT-23 Package Dimension Drawing



Notes:

1. Carrier tape: black conductive polycarbonate.
2. Cover tape material: transparent conductive PSA.
3. Cover tape size: 5.40 mm width.
4. Tolerance ± 0.10 mm.
5. Ten sprocket hole pitch cumulative tolerance: ± 0.2 mm.
6. All measurements are in millimeters.
7. Alternative carrier tape dimensions are:
 - Ao = 3.3
 - Bo = 2.9
 - Ko = 1.22

200041-011

Figure 9. SOT-23 Tape and Reel Dimensions

Copyright © 2002-2007, 2009-2016, 2018 Skyworks Solutions, Inc. All Rights Reserved.

Information in this document is provided in connection with Skyworks Solutions, Inc. ("Skyworks") products or services. These materials, including the information contained herein, are provided by Skyworks as a service to its customers and may be used for informational purposes only by the customer. Skyworks assumes no responsibility for errors or omissions in these materials or the information contained herein. Skyworks may change its documentation, products, services, specifications or product descriptions at any time, without notice. Skyworks makes no commitment to update the materials or information and shall have no responsibility whatsoever for conflicts, incompatibilities, or other difficulties arising from any future changes.

No license, whether express, implied, by estoppel or otherwise, is granted to any intellectual property rights by this document. Skyworks assumes no liability for any materials, products or information provided hereunder, including the sale, distribution, reproduction or use of Skyworks products, information or materials, except as may be provided in Skyworks Terms and Conditions of Sale.

THE MATERIALS, PRODUCTS AND INFORMATION ARE PROVIDED "AS IS" WITHOUT WARRANTY OF ANY KIND, WHETHER EXPRESS, IMPLIED, STATUTORY, OR OTHERWISE, INCLUDING FITNESS FOR A PARTICULAR PURPOSE OR USE, MERCHANTABILITY, PERFORMANCE, QUALITY OR NON-INFRINGEMENT OF ANY INTELLECTUAL PROPERTY RIGHT; ALL SUCH WARRANTIES ARE HEREBY EXPRESSLY DISCLAIMED. SKYWORKS DOES NOT WARRANT THE ACCURACY OR COMPLETENESS OF THE INFORMATION, TEXT, GRAPHICS OR OTHER ITEMS CONTAINED WITHIN THESE MATERIALS. SKYWORKS SHALL NOT BE LIABLE FOR ANY DAMAGES, INCLUDING BUT NOT LIMITED TO ANY SPECIAL, INDIRECT, INCIDENTAL, STATUTORY, OR CONSEQUENTIAL DAMAGES, INCLUDING WITHOUT LIMITATION, LOST REVENUES OR LOST PROFITS THAT MAY RESULT FROM THE USE OF THE MATERIALS OR INFORMATION, WHETHER OR NOT THE RECIPIENT OF MATERIALS HAS BEEN ADVISED OF THE POSSIBILITY OF SUCH DAMAGE.

Skyworks products are not intended for use in medical, lifesaving or life-sustaining applications, or other equipment in which the failure of the Skyworks products could lead to personal injury, death, physical or environmental damage. Skyworks customers using or selling Skyworks products for use in such applications do so at their own risk and agree to fully indemnify Skyworks for any damages resulting from such improper use or sale.

Customers are responsible for their products and applications using Skyworks products, which may deviate from published specifications as a result of design defects, errors, or operation of products outside of published parameters or design specifications. Customers should include design and operating safeguards to minimize these and other risks. Skyworks assumes no liability for applications assistance, customer product design, or damage to any equipment resulting from the use of Skyworks products outside of stated published specifications or parameters.

Skyworks and the Skyworks symbol are trademarks or registered trademarks of Skyworks Solutions, Inc. or its subsidiaries in the United States and other countries. Third-party brands and names are for identification purposes only, and are the property of their respective owners. Additional information, including relevant terms and conditions, posted at www.skyworksinc.com, are incorporated by reference.